Single-Sided Ultrasound Imaging of the Bone Cortex
Anatomy, Tissue Characterization and Blood Flow

Renaud, Guillaume; Salles, Sébastien

DOI
10.1007/978-3-030-91979-5_10

Publication date
2022

Document Version
Final published version

Published in
Advances in Experimental Medicine and Biology

Single-Sided Ultrasound Imaging of the Bone Cortex: Anatomy, Tissue Characterization and Blood Flow

10

Guillaume Renaud and Sébastien Salles

Abstract

In this chapter, we first review the reasons why conventional ultrasonography fails to image the interior of bones. Next we show our recent work on imaging a cortical bone layer with ultrasound. Revealing the shape of the cortex of a bone, in particular its thickness, is of interest for evaluating bone strength. In addition we describe how the process of reconstructing a truthful image of the bone cortex includes the estimation of ultrasound wave-speed in cortical bone tissue. Cortical bone exhibits elastic anisotropy, which causes anisotropy of ultrasound wave-speed as well. Therefore a faithful and high-quality picture of the bone cortex is obtained if wave-speed anisotropy is taken into account during image reconstruction. Capitalizing on prior knowledge on the elastic anisotropy of cortical bone, a procedure for estimating wave-speed and its anisotropy is described. It is based on the measurement of a head-wave velocity and an autofocus approach. The latter relies on the fact that the reconstructed ultrasound image shows optimal quality if the wave-speed model is correct. In order to achieve real-time imaging of a bone cortex, image reconstruction is performed with a delay-and-sum algorithm. Finally, we report recent advances in the measurement of blood flow in cortical bone.

Keywords

Ultrasound imaging · Cortical bone · Elastic anisotropy · Wave-speed estimation · Wave refraction · Blood flow

10.1 Introduction

The development in the past 20 years of synthetically-focused ultrasound imaging, which utilizes unfocused transmit beams (Jensen et al., 2006) instead of focused transmit beams (i.e. tradition ultrasound imaging), has enables new technologies, in particular shear-wave elastography (Montaldo et al., 2009) and ultrafast imaging of blood flow (Bercoff et al., 2011), thanks to the joint improvement of temporal resolution and synchronicity of the information estimated in the entire image. Synthetically-

G. Renaud (✉)
Sorbonne Université, CNRS UMR 7371, INSERM UMR S 1146, Laboratoire d'Imagerie Biomédicale, Paris , France

Department of Imaging Physics, Delft University of Technology, Delft , The Netherlands

S. Salles
Department of Imaging Physics, Delft University of Technology, Delft , The Netherlands

P. Laugier, Q. Grimal (eds.), *Bone Quantitative Ultrasound*, Advances in Experimental Medicine and Biology 1364, https://doi.org/10.1007/978-3-030-91979-5_10

focused ultrasound imaging has also greatly improved the versatility of ultrasound imaging. Because the transmission of a spherical or plane wave does not require any assumption about the medium, it enables the modeling of more complex ultrasound physics during image reconstruction, just like in seismic imaging.

Ultrasound imaging has long been considered incapable of imaging the inner structure of bones. However, the advent of synthetically-focused ultrasound imaging together with the continuous improvement of electronics quality, transducer sensitivity and computer processing power has recently enabled intraosseous ultrasound imaging. In this book chapter, we will show that ultrasound imaging of bones can provide three types of information:

- Anatomy, in particular the thickness of the cortex of long bones, which is useful for estimating the mechanical strength of a bone;
- Tissue characterization thanks to the estimation of ultrasound wave-speed and its anisotropy in cortical bone, which carry information about its overall porosity as well as its nano- and micro-structure;
- Intraosseous blood flow, which is a key actor in bone growth and remodeling, bone metabolism, fracture healing and joint diseases.

10.2 Why Does Conventional Ultrasonography Fail to Image the Inside of a Bone?

Ultrasound imaging is extensively used for the examination of soft tissues. Although ultrasound imaging was shown to accurately image the outer surface of bones and thus allowing for the diagnosis of suspected bone fractures (Beltrame et al., 2012), current clinical ultrasound scanners fail to reveal the inner structure of bones. Conventional ultrasound imaging relies on the transmission of a series of focused narrow ultrasound beams, the recording of echoes reflected in the medium and an algorithm of image reconstruction (Hoskins et al., 2019; Shung, 2015; Szabo, 2013). The logical basis in conventional ultrasound imaging is to sequentially reconstruct straight lines in the image, by selectively insonifying the scatterers that are located on a given image line. The selective insonification of each image line is performed by transmitting a series of focused narrow ultrasound beams, as many beams as the number of lines in the image. This approach provides optimal contrast resolution in the image. An ultrasound probe contains an array of individual active elements, usually made of a piezoelectric material, that are able to generate and record ultrasound waves. Such an array transducer can generate a transmit focused beam by delaying the excitation of individual elements.

The reconstruction of each image line is traditionally done as follows (Fig. 10.1):

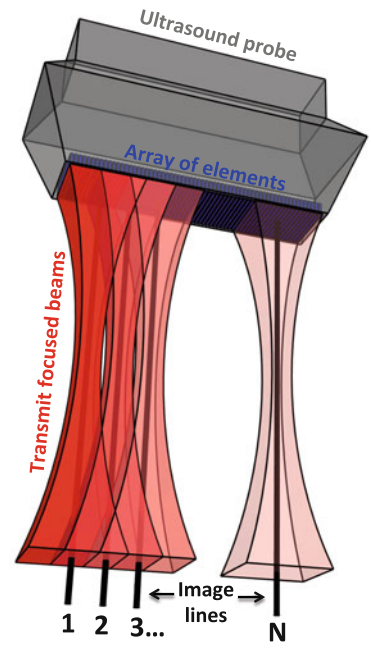

Fig. 10.1 Sequential transmission of focused narrow beams as used in conventional cross-sectional (2D) ultrasound imaging. This 2D image would be made of N lines, N focused beams are then successively generated

1. Transmission of a focused beam whose axis coincides with the image line, by delaying the excitation of individual elements of the array (the calculation of the transmit delays relies on the prior knowledge of the wave-speed in the medium and assumes a homogeneous medium)
2. Recording of echo signals by a receive aperture (group of elements in the probe array selected for recording)
3. For each image point (or pixel) on this line, and for all elements of the receive aperture, calculation of the expected arrival time of an echo signal generated by a point scatterer located at the coordinates of the image point (assuming medium is homogeneous and wave-speed is known)
4. The values of the recorded echo signals evaluated at specific instants (the calculated round-trip travel times) are summed over the receive aperture
5. Detection of the envelope of the reconstructed line for display (amplitude of the envelope is converted to pixel intensity in the displayed image)
6. Repeat procedure for next image line

This image reconstruction algorithm is called delay-and-sum (or shift-and-add) and is used in most ultrasound scanners. Figure 10.2 illustrates the principle of a delay-and-sum algorithm. It can be shown that this operation is analog to a back-propagation of the recorded echo signals towards the scatterers in the medium (Liu & Waag, 1997).

In current clinical ultrasound scanners, the calculation of both transmit delays (to generate a focused beam) and the round-trip travel times (for image reconstruction) assumes a simplified medium with a uniform speed of sound, equal to the average value in soft tissues (1540 m/s). This assumption is acceptable in soft tissues because the difference between the average value and the

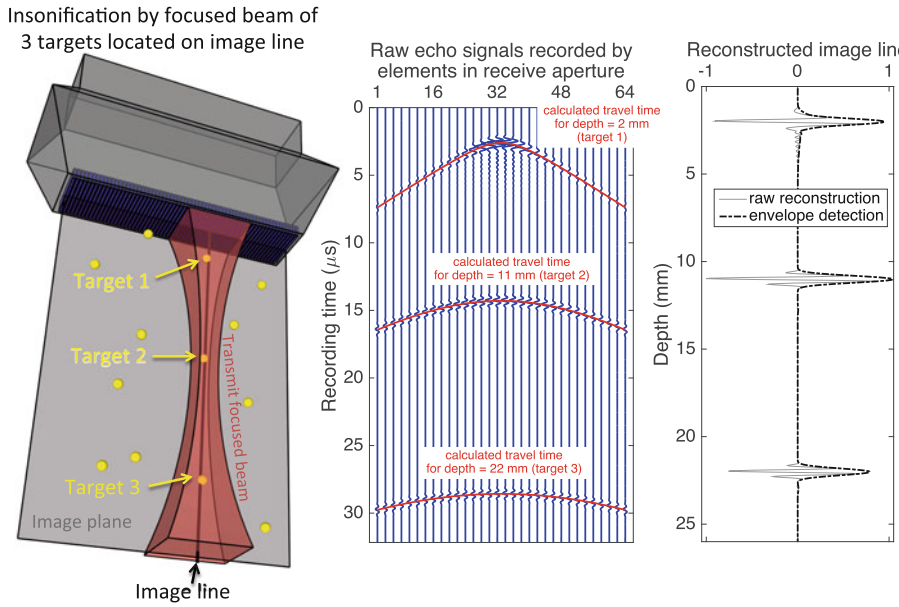

Fig. 10.2 Reconstruction of one image line with a delay-and-sum algorithm in conventional ultrasound imaging. Among the objects (yellow spheres) located in the image plane, 3 are located very close to the image line. Thanks to the transmit focused beam, only these 3 targets create echo signals. The calculated round-trip travel times at the exact three depths of the targets are depicted, it is seen that they overlap perfectly with the echo signals recorded by the receive aperture. The delay-and-sum algorithm converts these 3 echo signals into a single image line. Its amplitude (envelope) is then converted into pixel intensity for display

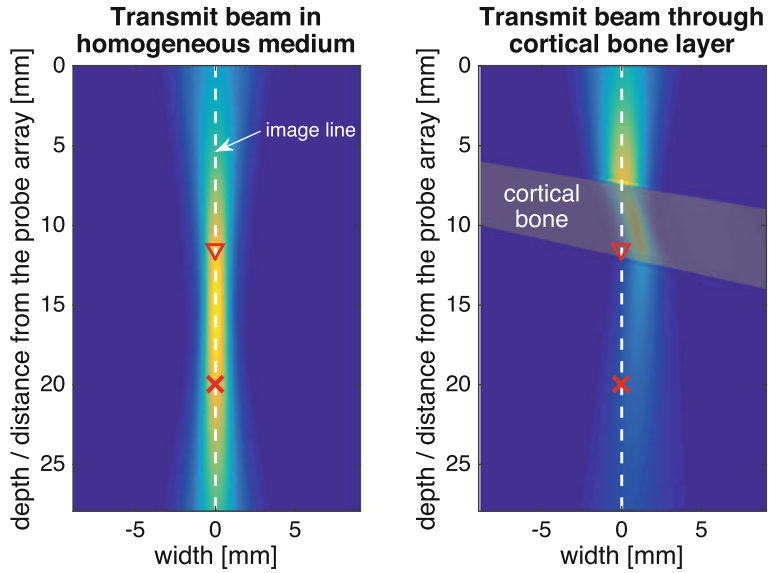

Fig. 10.3 Effect of the bone cortex on a transmit focused ultrasound beam as generated in conventional ultrasonography. For each image line (shown by the vertical dashed line), a focused beam is transmitted along the image line. The objective is to insonify only targets located on the image line, in principle this ensures optimal image contrast. The complete image is obtained by repeating the procedure for all image lines. It is seen that the layer of cortical bone deviates (refraction) the transmit beam from the image line. The round-trip travel times for the two points indicated by a triangle and a cross are calculated in Fig. 10.4. The wave-speed in soft tissue and in cortical bone is 1540 and 3500 m/s

true speed of sound is at most $\pm 10\%$. However this assumption does not hold for cortical bone that forms the cortex (outer shell) of bones. The compression wave-speed in cortical bone is much larger (2800–4200 m/s, Granke et al., 2011) than that in soft tissues (1400–1700 m/s, Shung, 2015), which leads to substantial refraction when an ultrasound wave traverses an interface between soft tissue and cortical bone. The physics of refraction tells us that the propagation direction of a wave changes when traversing an interface between two media with a different speed of sound. Therefore refraction corrupts both the transmit focused beam (Fig. 10.3) and the calculation of the round-trip travel times (Fig. 10.4). As a result, the objects located behind (deeper than) the first interface between soft tissue and bone appear blurred, with a weak intensity and at a wrong spatial location, in an image reconstructed by current clinical scanners.

There exist two other assumptions used in conventional ultrasonography. Namely, the medium is described as a fluid with isotropic compression wave-speed and multiple scattering is ignored. While acceptable in soft tissues, they do not hold in bones. As a matter of fact, cortical bone is a solid elastic material with anisotropic elasticity, which results in anisotropy of wave-speed (Sect. 10.3). In addition, shear waves can be generated by mode-conversion as an ultrasonic wave enters cortical bone, and can be reflected inside the cortex of a bone (Sect. 10.4). Finally the large mismatch in acoustic impedance between cortical bone and soft tissues favors the generation of multiple scattering, between the ultrasound probe and a bone or within the cortex of a bone. Multiple scattering and mode-converted shear-waves create clutter in the ultrasound image of a bone and degrade contrast resolution.

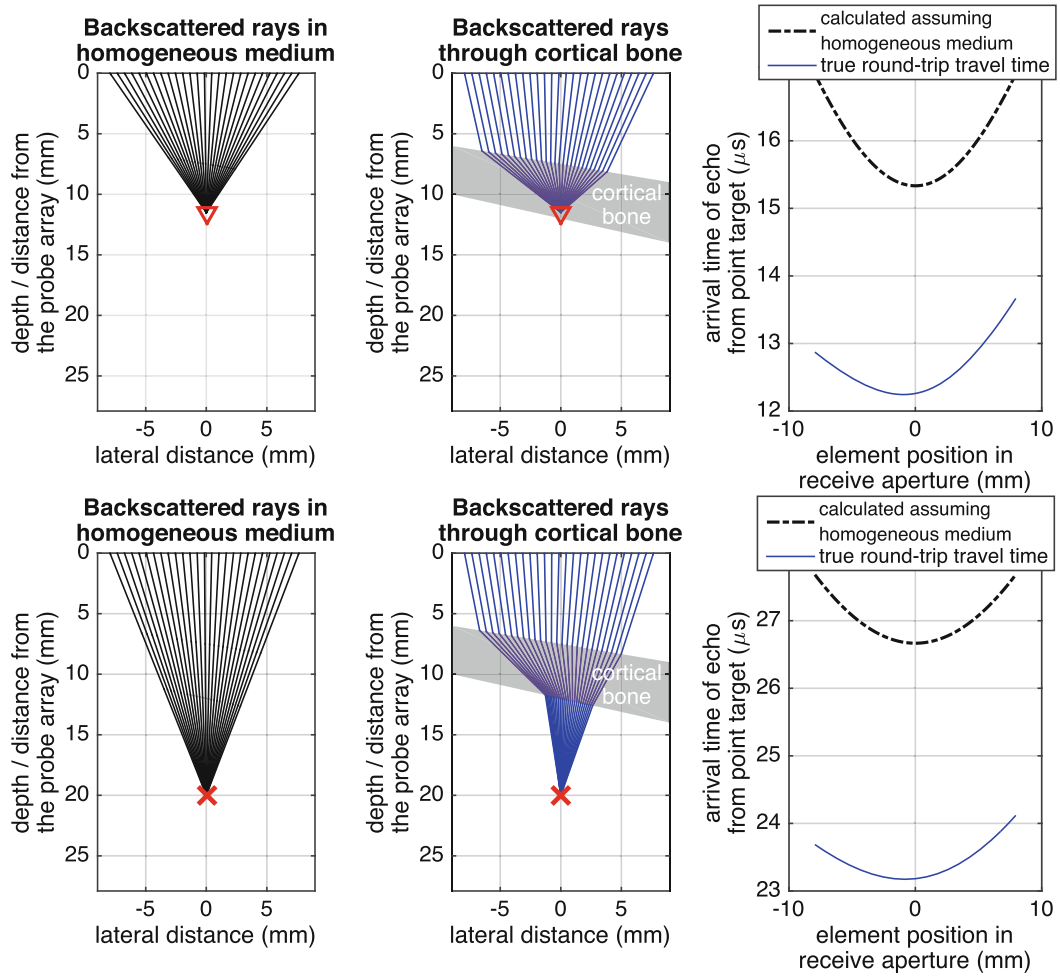

Fig. 10.4 Effect of the bone cortex on the backscattered rays for a point target in the cortical bone layer (top panels) and another one beneath the bone cortex (bottom panels). For both targets, conventional ultrasonography leads to erroneous calculation of round-trip travel times, which results in sub-optimal image reconstruction

10.3 Elastic Anisotropy of Cortical Bone and Wave-Speed Anisotropy

In this chapter, ultrasound in the 1–5 MHz range is considered, which corresponds to a wavelength in the 0.6–4 mm range for a compression wave, and in the 0.3–2 mm for a shear wave. The elastic anisotropy of cortical bone sensed by such ultrasonic waves is determined at two scales by two features, namely the orientation of mineralized collagen fibers constituting the solid phase of cortical bone and the Haversian canals (created by bone remodeling) hosting blood vessels and nerves (Rho et al., 1998). In the cortex of the diaphysis of a long bone, the Haversian canals (approximately cylindrical pores, ~100 μm in diameter) are nearly aligned with the axis of the long bone, which causes elastic anisotropy at the scale of a few millimeters (Parnell & Grimal, 2009). In addition, the complicated organization of mineralized collagen fibers results in elastic anisotropy at the scale of a few hundreds of micrometers (Cai et al., 2020; Rohrbach et al., 2012). In other words, the elasticity of the solid phase of bone (the bone matrix) is anisotropic, which also contributes to elastic anisotropy at

the scale of a few millimeters. The elasticity of human cortical bone is in general well described with a model of transverse isotropy (or hexagonal symmetry) (Yoon & Katz, 1976; Bernard et al., 2016; Granke et al., 2011, see also Chap. 13 in this book). Several studies have reported measurements showing orthotropic elasticity of human cortical bone, in particular at proximal and distal diaphyseal regions of a long bone (Ashman et al., 1984; Rho, 1996; Rudy et al., 2011). However the degree of orthotropic symmetry was rather small, thus a model of transverse isotropy is a reasonable approximation of the elasticity of human cortical bone.

The stress components σ_{ij} can be related to the strain components ϵ_{ij} via the elasticity tensor which can be written in a matrix form C_{ij}. In a material with transverse isotropy, C_{ij} has five independent components. This relation is often specified in a basis with a coordinate axis aligned with the symmetry axis in the material. For instance, with coordinate axis 3 aligned with the symmetry axis, it can be written:

$$\begin{pmatrix} \sigma_{11} \\ \sigma_{22} \\ \sigma_{33} \\ \sigma_{23} \\ \sigma_{13} \\ \sigma_{12} \end{pmatrix} = \begin{pmatrix} C_{11} & C_{11}-2C_{66} & C_{13} & 0 & 0 & 0 \\ C_{11}-2C_{66} & C_{11} & C_{13} & 0 & 0 & 0 \\ C_{13} & C_{13} & C_{33} & 0 & 0 & 0 \\ 0 & 0 & 0 & C_{44} & 0 & 0 \\ 0 & 0 & 0 & 0 & C_{44} & 0 \\ 0 & 0 & 0 & 0 & 0 & C_{66} \end{pmatrix} \begin{pmatrix} \epsilon_{11} \\ \epsilon_{22} \\ \epsilon_{33} \\ 2\epsilon_{23} \\ 2\epsilon_{13} \\ 2\epsilon_{12} \end{pmatrix}$$

In a material with hexagonal symmetry, three types of bulk elastic waves can exist: a quasi-compression wave with quasi-longitudinal polarization (or quasi P-wave), a quasi-shear wave with quasi-vertical polarization (or quasi SV-wave), and a pure shear wave with horizontal polarization (or SH-wave). Conventional derivation of the phase velocities of bulk elastic waves involves the elastic stiffnesses C_{ij} and mass density ρ (Auld, 1973a). There exist other formulations, in particular Thomsen (Thomsen, 1986) proposed to recast the expressions of phase velocities of bulk elastic waves using wave-speeds in specific orientations. The compression phase velocity v_P and the shear phase velocity with vertical polarization v_{SV} and the shear phase velocity with horizontal polarization v_{SH} are given by:

$$v_P(\theta) = \alpha_0 \left[1 + \varepsilon \cos^2(\theta) + D^*\left(\theta, \alpha_0, \beta_0, \varepsilon, \delta^*\right) \right]^{1/2} \tag{10.1}$$

$$v_{SV}(\theta) = \beta_0 \left[1 + \left(\frac{\alpha_0^2}{\beta_0^2}\right)\left(\varepsilon \cos^2(\theta) - D^*\left(\theta, \alpha_0, \beta_0, \varepsilon, \delta^*\right)\right) \right]^{1/2} \tag{10.2}$$

$$D^* = \frac{1}{2}\left(1 - \frac{\beta_0^2}{\alpha_0^2}\right) \times \left[\left(1 + \frac{4\delta^* \cos^2(\theta)\sin^2(\theta)}{(1-\beta_0^2/\alpha_0^2)^2} + \frac{4(1-\beta_0^2/\alpha_0^2+\varepsilon)\varepsilon}{(1-\beta_0^2/\alpha_0^2)^2}\cos^4(\theta) \right)^{1/2} - 1 \right] \tag{10.3}$$

$$v_{SH}(\theta) = \beta_0\left[1 + 2\gamma\cos^2(\theta)\right]^{1/2} \tag{10.4}$$

$$\alpha_0 = \sqrt{\frac{C_{33}}{\rho}} \tag{10.5}$$

$$\beta_0 = \sqrt{\frac{C_{44}}{\rho}} \tag{10.6}$$

$$\varepsilon = \frac{C_{11} - C_{33}}{2C_{33}} \tag{10.7}$$

$$\delta^* = \frac{1}{2C_{33}^2}\Big(2(C_{13} + C_{44})^2 - (C_{33} - C_{44})(C_{11} + C_{33} - 2C_{44})\Big) \tag{10.8}$$

$$\gamma = \frac{C_{66} - C_{44}}{2C_{44}} \tag{10.9}$$

α_0 and β_0 are the phase velocity of a compression wave and a shear wave with vertical polarization in the direction of the symmetry axis. ε and δ^* are two parameters of anisotropy. θ is the phase angle between the wave vector and the plane of isotropy. As illustrated in Fig. 10.5, the axis of symmetry of human diaphyseal cortical bone is nearly aligned with the long bone axis. The plane (1,2) (or any plane parallel to it) is a plane of isotropy in which the velocity of a compression or shear wave does not depend on the propagation direction.

Using ex vivo resonant ultrasound spectroscopy (RUS) measurements reported by colleagues (Bernard et al., 2016; Cai et al., 2017, 2019, see also Chaps. 12and 13 in this book), it is possible to calculate α_0, β_0, ϵ and δ^* (Fig. 10.6). Human cortical bone samples with a mass density between 1800 and 2000 kg/m^3 were selected (corresponding to a porosity between 2 and 20%). The 220 selected samples were taken from the tibia, the femur or the radius of donors (50–95 years old). The median values of α_0, β_0, ε, δ^* and γ are 3.9 mm/μs, 1.8 mm/μs, −0.18, −0.15 and −0.15, respectively.

For ultrasound image reconstruction, one needs the group velocity V (or ray velocity) and group angle ϕ (or ray angle), they can be calculated as follows (Thomsen, 1986):

$$\tan\Big(\phi(\theta)\Big) = \left(\tan\theta + \frac{1}{v}\frac{\partial v}{\partial\theta}\right)\Big/ \left(1 - \frac{\tan\theta}{v}\frac{\partial v}{\partial\theta}\right) \tag{10.10}$$

$$V^2\Big(\phi(\theta)\Big) = v^2(\theta) + \left(\frac{\partial v}{\partial\theta}\right)^2 \tag{10.11}$$

v is the phase velocity of a shear or a compression wave, θ is the corresponding phase angle.

Using the median values of Thomsen's parameters calculated from RUS measurements, the group velocity was computed (Carcione, 2014) and is shown in Fig. 10.7. It is seen that the group velocity of a compression wave and a shear wave with horizontal polarization has a minimum value in the plane of isotropy and peaks in the direction of the symmetry axis. The group velocity of a shear wave with vertical polarization equals β_0 in the direction of the symmetry axis and a direction normal to it. For intermediate angles, its velocity can be larger or smaller than β_0, depending on the values of δ^* and ε, and the maximum (or minimum) is observed for a group angle close to 40°.

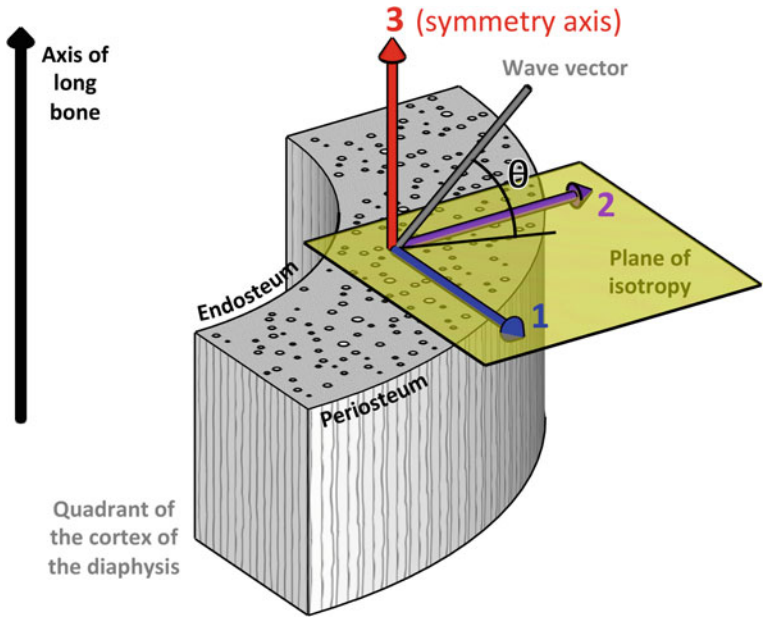

Fig. 10.5 Simplified representation of a quadrant of the cortex of the diaphysis of a long bone. Pores are simplified as cylindrical cavities, aligned with the long bone axis. Coordinate axis 3 is aligned with the symmetry axis of the material, which is nearly aligned with the long bone axis. The plane (1,2) (or any plane parallel to it) is a plane of isotropy. θ is the phase angle between the wave vector and the plane of isotropy

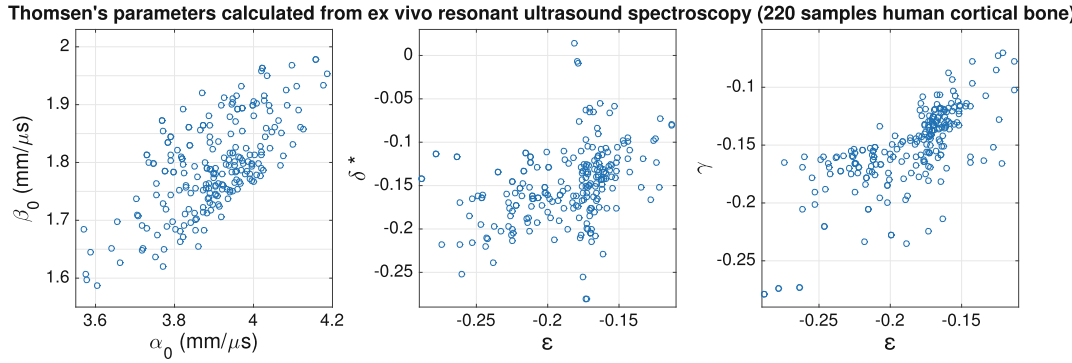

Fig. 10.6 Thomsen's parameters calculated from ex vivo resonant ultrasound spectroscopy measurements on 220 samples of human cortical bone (compilation of data from Bernard et al. (2016), Cai et al. (2017), Cai et al. (2019)). The median values of α_0, β_0, ε, δ^* and γ are 3.9 mm/µs, 1.8 mm/µs, −0.18, −0.15 and −0.15, respectively

Figure 10.7 shows the polarization, i.e. the direction of the displacement of the matter resulting from the passage of the ultrasound wave, of the compression wave and the two types of shear waves. Because of elastic anisotropy, it is seen that the polarization of a compression wave in a plane parallel to the symmetry axis is quasi longitudinal, i.e. not exactly parallel to the acoustic ray. Similarly the vertical polarization of a shear wave is quasi transverse, i.e. not exactly normal to the acoustic ray. However, the horizontal polarization of a shear wave is exactly normal to the acoustic ray (pointing out of the page).

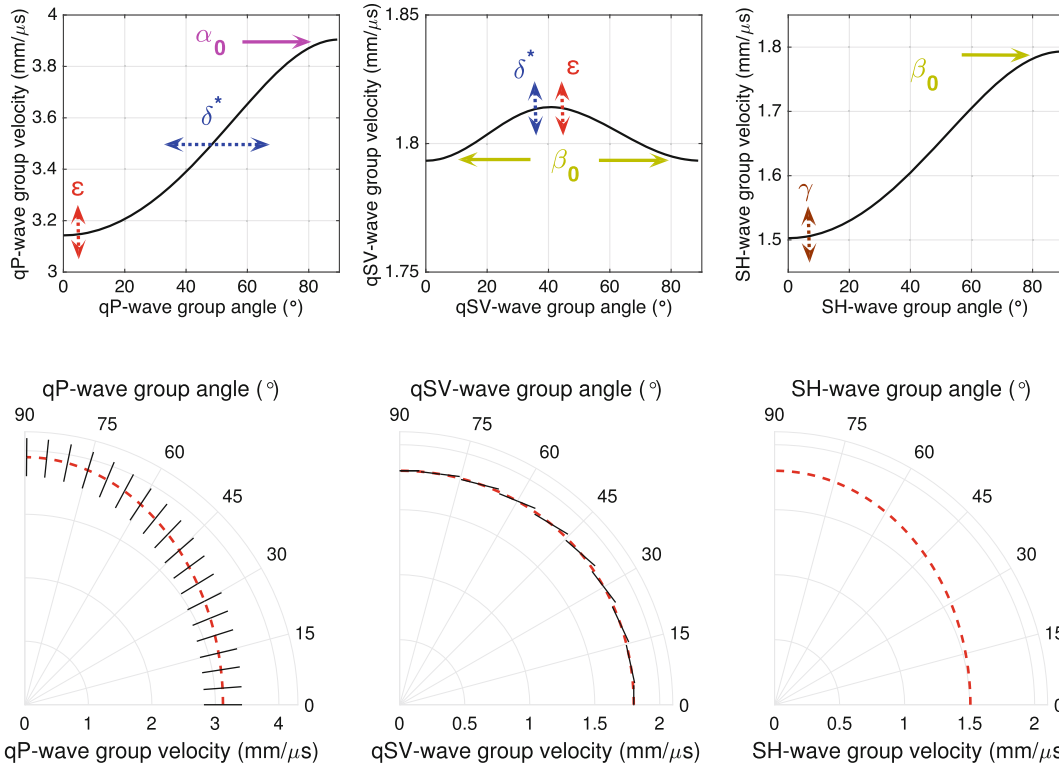

Fig. 10.7 Anisotropy of the group velocity of a quasi P-wave, quasi SV-wave and SH-wave in human cortical bone calculated with median values of Thomsen's parameters reported in Fig. 10.6. It is indicated how Thomsen's parameters influence the anisotropy. The polarization directions are indicated (the SH polarization is normal to the plane of the page)

10.4 Transmission and Reflection of a Pulsed Wave in the Cortex of a Bone

In this chapter, we consider the use of a conventional clinical ultrasound transducer array. Such a transducer contains a linear array of piezoelectric elements for two-dimensional imaging. Most common ultrasound transducers are either linear arrays with a spatial period (or pitch) close to one wavelength (in soft tissues) or phased arrays with a spatial period close to half a wavelength (in soft tissues) (Hoskins et al., 2019; Shung, 2015; Szabo, 2013). Because of grating lobes, optimal beam steering angles should not exceed 30° with a linear array, while steering angles up to 60° can be used with a phased-array transducer. The probe will be either aligned with the long bone axis to make a longitudinal-view image, or positioned normal to the long bone axis to make a transverse-view image. Here we review the types of wave paths encountered as the transducer broadcasts a wave that enters the bone cortex, reflects at the inner surface (endosteum) and returns to the probe array. Figure 10.8 illustrates the four types of ray paths considered here:

- the "PP" path: reflection of the compression wave broadcasted by the emitting element at the outer surface of the bone cortex (periosteum)
- the "PPPP" path: reflection of the compression wave broadcasted by the emitting element at the inner surface of the bone cortex (endosteum), without mode conversion

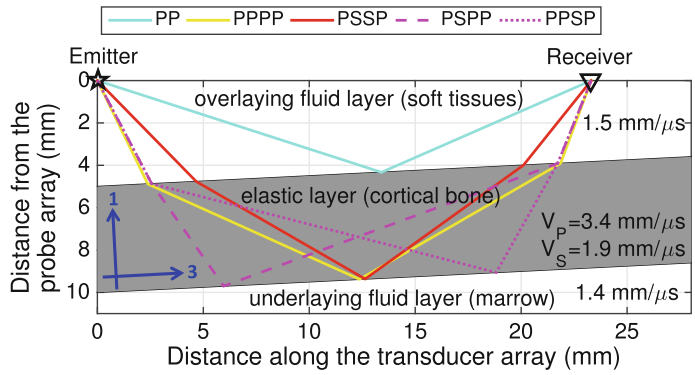

Fig. 10.8 Illustration of ray paths considered in this work. The situation depicted in the figure corresponds to a transmission with an element of the probe array and reception with a different element. The four paths are labeled with *P* and *S* referring to a compression wave and a shear wave, respectively. In this illustration, the elastic layer has isotropic elasticity with a compression wave-speed of 3.4 mm/μs and a shear wave-speed of 1.9 mm/μs. The speed of sound in the overlaying and underlaying fluid layers is 1.5 and 1.4 mm/μs

- the "PSSP" path: reflection of the compression wave broadcasted by the emitting element at the inner surface of the bone cortex (endosteum), without mode conversion during reflection but with mode conversion (compression wave to shear wave and then shear wave to compression wave) during transmission/refraction at the outer surface of the bone cortex (periosteum)
- the "PSPP/PPSP" path: reflection of the compression wave broadcasted by the emitting element at the inner surface of the bone cortex (endosteum), with mode conversion during reflection and during transmission/refraction at the outer surface of the bone cortex (periosteum) (compression wave to shear wave or shear wave to compression wave)

Next, it is informative to calculate the reflection and transmission power coefficients in the different scenarios encountered when imaging the cortex with ultrasound, as shown in Fig. 10.8. With a clinical array transducer designed for two-dimensional imaging, the diaphysis of a long bone is ideally imaged in a plane of isotropy (transverse view) or in a plane containing the bone axis (longitudinal view). Therefore we evaluated the power coefficients in these two situations by imposing continuity of the displacement vector and traction forces on the interface (Aki & Richards, 2002; Auld, 1973b; Carcione, 2014). An interface between a fluid half space (soft tissue) and a second half space of cortical bone is considered. The median values of Thomsen's parameters (Fig. 10.6) and a mass density of 1.92 g/cm^3 was used for cortical bone. For the fluid half space, we used a wavespeed of 1.5 mm/μs and a mass density of 1 g/cm^3. Figure 10.9 shows the results for an incident plane wave. Note that for an incident spherical wave, the calculations shown in Fig. 10.9 will be slightly modified due to the curvature of the wavefront (Brekhovskikh & Godin, 1992; Ursenbach et al., 2005; Aki and Richards, 2002).

Several important facts can be learned from Fig. 10.9. There can exist two critical angles, related to the compression and shear wave-speeds in cortical bone. In particular, an incident P-wave in the fluid is able to transmit a P-wave in cortical bone, only if the incident angle does not exceed the critical angle $\arcsin\left[V_{fluid}/\alpha_0\right]$ (longitudinal plane) or $\arcsin\left[V_{fluid}/(\alpha_0\sqrt{1+2\varepsilon})\right]$ (transverse plane), where V_{fluid} is the compression wave-speed in the fluid. When implementing plane wave imaging, it is thus crucial to generate plane wavefronts in the soft tissue surrounding bone with incident angles smaller than 20°. In a longitudinal plane, an incident P-wave in the fluid is able to transmit a SV-wave in cortical

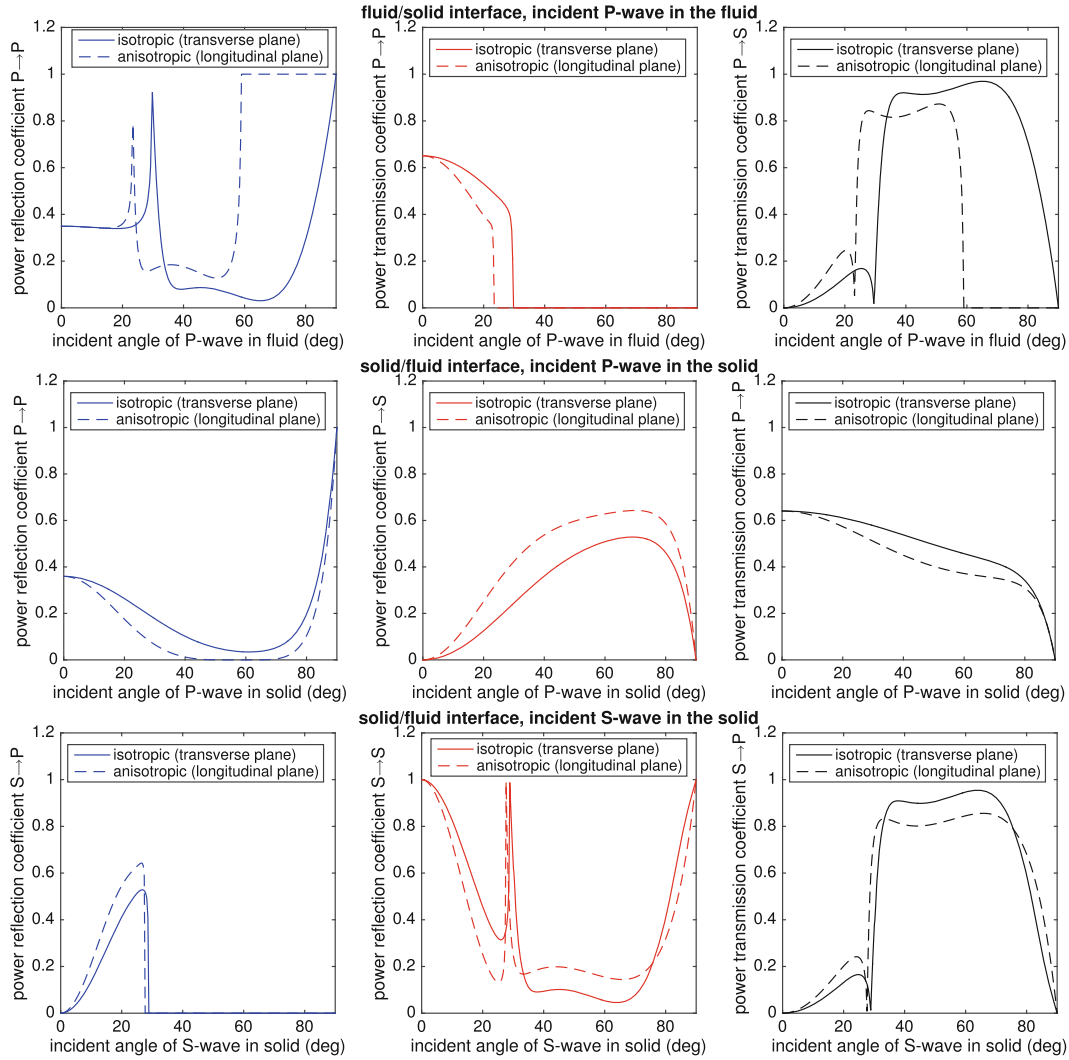

Fig. 10.9 Power reflection and transmission coefficients for an incident plane wave (P-wave or S-wave) calculated at an interface between cortical bone and soft tissue

bone, only if the incident angle does not exceed the critical angle close to $\arcsin\left[V_{fluid}/\beta_0\right]$. Also noteworthy, but not shown in Fig. 10.9, the coefficients of reflection and transmission become complex for incident angles exceeding the first critical angle, which means that the phase of the reflected or transmitted wave is modified (compared to the incident waveform). This feature is of importance when applying the autofocus method (see Sect. 10.7). For an incident S-wave in cortical bone, a reflected P-wave generated by mode-conversion only exists for an incident angle smaller than approximately $\arcsin\left[\beta_0/\alpha_0\right]$ (longitudinal plane) or $\arcsin\left[(\beta_0\sqrt{1+2\gamma})/(\alpha_0\sqrt{1+2\varepsilon})\right]$ (transverse plane). As a consequence, the PSPP path (see Fig. 10.8) has a significant amplitude (recorded by the probe array) only for small incidence angles (smaller than 25° at the endosteum).

In the case of a transmit spherical (or cylindrical) beam, it is possible to observe head waves, also known in the literature as "lateral waves" or "conical waves" (Aki & Richards,

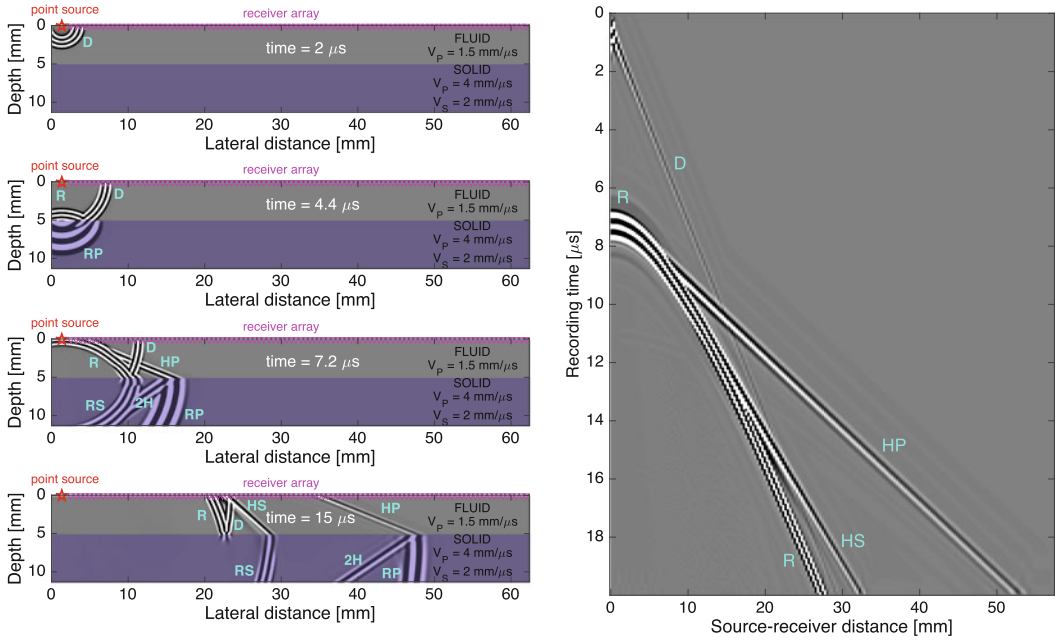

Fig. 10.10 Interaction of a cylindrical wave with a plane interface separating a fluid half-space and a solid elastic half-space. Synthetic signals were generated with a time-domain finite-difference wave equation solver (Bossy et al., 2002). D: direct wave, R: specularly reflected wave, RP: refracted P-wave, RS: refracted S-wave, HP: first kind compression head-wave, HS: first kind shear head-wave, 2H: second kind compression head-wave. The source broadcasts a tapered waveform with 3 cycles at 2.5 MHz

2002; Brekhovskikh & Godin, 1992; Cerveny, 2001). As proposed by seismologists, although this signal has a weak amplitude, it can be exploited to measure the wave-speed in the layer under the interface (Telford et al., 1990b). The head wave cannot be mathematical obtained with zeroth-order ray theory. An asymptotic high-frequency treatment of the integral representation of the spherical wave is necessary. The simplest situation to consider is a spherical wave generated by a point source, incident at a plane interface between two homogeneous fluid half-spaces noted 1 and 2, with wave-speeds c_1 and c_2. The head wave exists only if the source is located in the half-space with the smallest wave-speed (for instance source in half-space 1, $c_2 > c_1$), and if the source-receiver distance is larger than a critical distance determined by the critical angle $\arcsin(c_1/c_2)$. The energy associated with the head wave comes from the first-order correction term of the refracted wave, which exists only with curved wavefronts.

We generated synthetic signals with a time-domain finite-difference elastic wave equation solver (Bossy et al., 2002, SimSonic software available at http://www.simsonic.fr/) to illustrate the richness of phenomena occurring as a cylindrical wave impacts an interface between a fluid half-space and a solid half-space (Fig. 10.10), and a solid elastic plate surrounded by two fluid half-spaces (Fig. 10.11). Interestingly, these synthetic signals greatly help to understand the echo signals acquired in vivo. As an example, Fig. 10.12 shows raw echo signals recorded in vivo at the tibial diaphysis with a phased array transducer aligned with the bone axis.

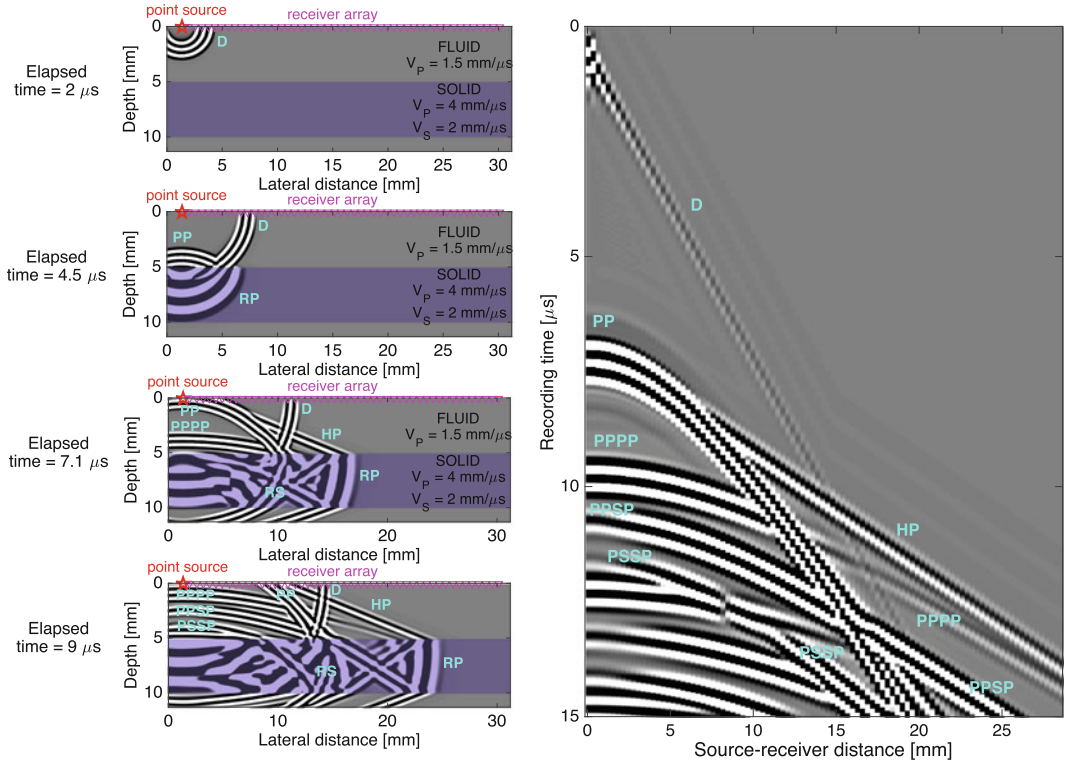

Fig. 10.11 Interaction of a cylindrical wave with a 5-mm thick elastic plate immersed in a fluid. Synthetic signals were generated with a time-domain finite-difference wave equation solver (Bossy et al., 2002). D: direct wave, RP: refracted P-wave, RS: refracted S-wave, HP: first kind compression head-wave. The labeled ray paths PP, PPPP, PPSP and PSSP are defined in Fig. 10.8. The source broadcasts a tapered waveform with 3 cycles at 2.5 MHz

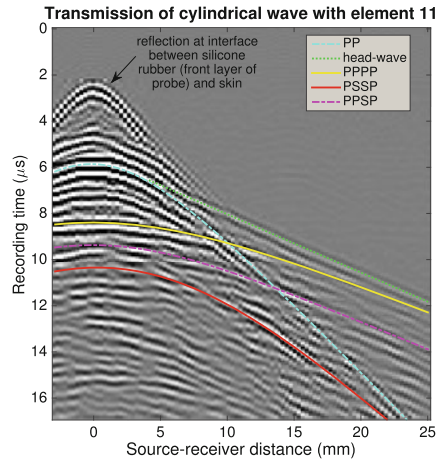

Fig. 10.12 Example of raw echo signals recorded in vivo at the tibia (middle of the diaphysis) when the probe is aligned with the bone axis (longitudinal plane). The acquisition was performed with a phased array transducer with 96 elements. The center frequency of the transmit short burst is 2.5 MHz. The figure shows the echo signals acquired after element 11 was excited to generate a cylindrical wave. The arrival times of head-wave and the 4 main ray paths PP, PPPP, PPSP and PSSP (as defined in Fig. 10.8) are indicated. Data reprocessed from Renaud et al. (2018b)

10.5 Image Reconstruction with Unfocused Transmit Beams

We have shown in Sect. 10.2 why conventional ultrasound imaging with transmit focused beams is inappropriate for imaging bone. This section shows that the transmission of unfocused ultrasound beams together with a reconstruction algorithm of synthetic focusing (in transmit and receive) is a better alternative. Two types of unfocused beams are typically considered because easy to describe mathematically: plane waves and cylindrical (or spherical) waves (Fig. 10.13).

It is possible to reconstruct an image with the transmission of a single unfocused wave in order to achieve excellent temporal resolution, however the resulting image shows poor contrast resolution compared to that achieved with conventional ultrasound imaging with transmit focused beams (Montaldo et al., 2009). In soft tissues, it was demonstrated that the transmission of multiple plane waves (with different steering angles) or multiple diverging spherical waves (with different point sources) can provide the same image quality (same contrast resolution) as with transmit focused beams (Montaldo et al., 2009). The combination of the low-contrast-resolution images (as many as transmit unfocused beams) into one high-contrast-resolution image is typically operated as a coherent summation (coherent compounding) (Montaldo et al., 2009).

Intraosseous ultrasound imaging shares many aspects with seismic imaging of the subsurface of the Earth. In particular, seismic exploration employs most often point sources, because the source size is smaller than the wavelength. The use of point sources was also proposed for medical ultrasound imaging. The point sources can be either physical or virtual. Physical point sources are simply obtained by exciting a single element of the array of an ultrasound transducer (Jensen et al., 2006), the width of an element is typically one wavelength or half a wavelength. Virtual point sources are generated with transmit delays, they can be placed either in front of the probe array (in the imaged medium) or behind the probe array (Nikolov & Jensen, 2002).

Image reconstruction in medical ultrasound is most often based on the *Delay-and-sum* algorithm (also called *Kirchhoff migration* in seismic imaging, see for instance Shearer (2009), or *Total focusing method* in non-destructive testing, see for instance Holmes et al. (2005)). Each image pixel is considered as a hypothetical scattering point. The reconstruction algorithm operates as a double summation of the recorded echo signals $D\left[t,\ iT,\ iR\right]$: (1) over the receive aperture of the transducer array of the recorded echo signals evaluated at the calculated round-trip travel times, and (2) over the transmissions (coherent compounding):

$$Image(x,z) = \sum_{iT=1}^{N_T}\sum_{iR=1}^{N_R} W(x,z,iT,iR) \times D\left[t = t_T(iT,x,z) + t_R(iR,x,z),\ iT,\ iR\right] \tag{10.12}$$

x and z are the cartesian coordinates of the pixel in the image. N_T and N_R are the number of transmit unfocused beams and the number of receive elements, respectively. $W(x,z,iT,iR)$ is a weighting function. Transmit and receive travel times, t_T and t_R are calculated with prior knowledge (or assumption) about the wave-speed in the medium. Figure 10.13 illustrates the procedure of synthetic focusing with transmit unfocused beams. Finally, after applying the delay-and-sum algorithm, the envelope of the high-resolution image is computed and most often log-compressed for display.

The delay-and-sum algorithm is in fact a point-diffractor (or scatter-point) imaging technique. However, as shown by seismologists who exten-

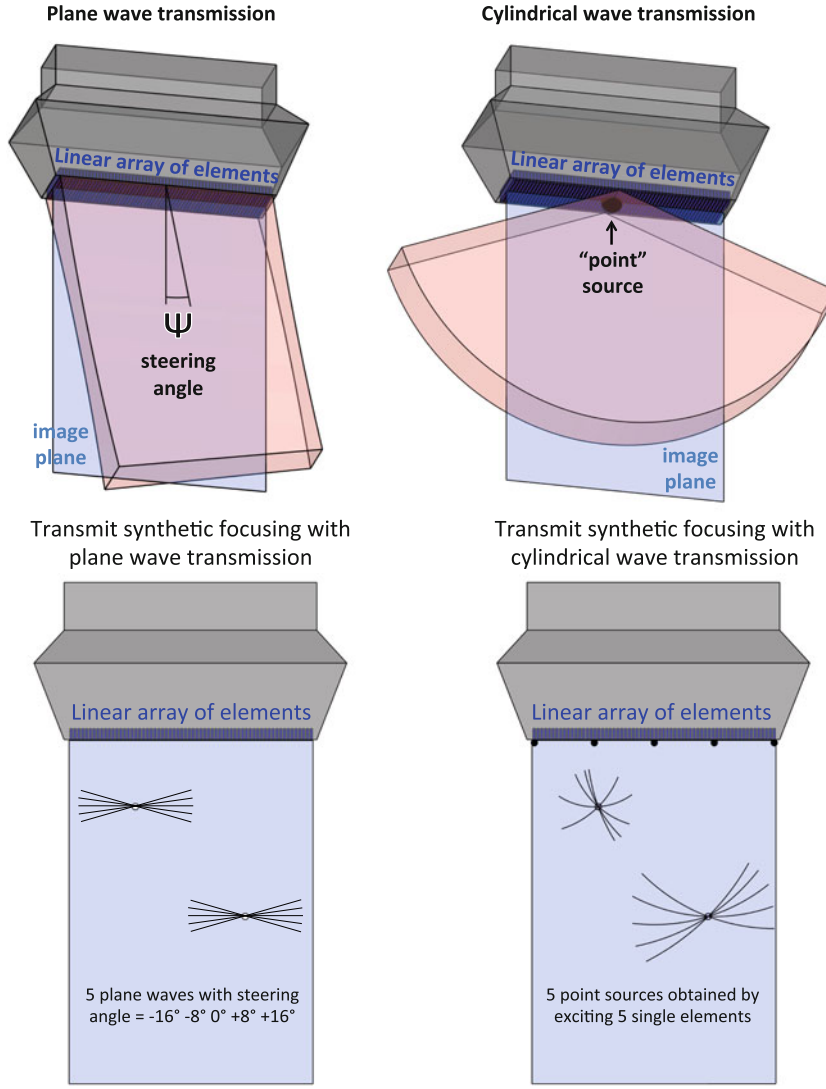

Fig. 10.13 Transmit unfocused beams for synthetically focused ultrasound imaging. The procedure of synthetic focusing is illustrated for two points in the image. Left: transmission of steered plane waves with different steering angles. Right: transmission of cylindrical waves with different point sources

sively studied Kirchhoff migration (Etgen et al., 2009), an interface can be seen as a large number of point-diffractors next to each other. In fact, the response of an interface can be described as the sum of the responses of many diffracting points along the interface. Thus the imaging technique performs well with specular reflections generated by interfaces in the medium.

Figures 10.14 and 10.15 show in vivo longitudinal and transverse images of the diaphysis of a tibia. The acquisition scheme allowed us to reconstruct the images either with 96 transmit cylindrical waves or 96 transmit plane waves. It is clear that cylindrical and plane transmit wavefronts produce similar images. Interestingly, the reconstruction using only 10 plane waves does not significantly degrade image quality. This fact can be advantageously exploited for real-time imaging (see Sect. 10.6). In Figs. 10.14 and 10.15, the periosteum is located at a depth of 3–4 mm.

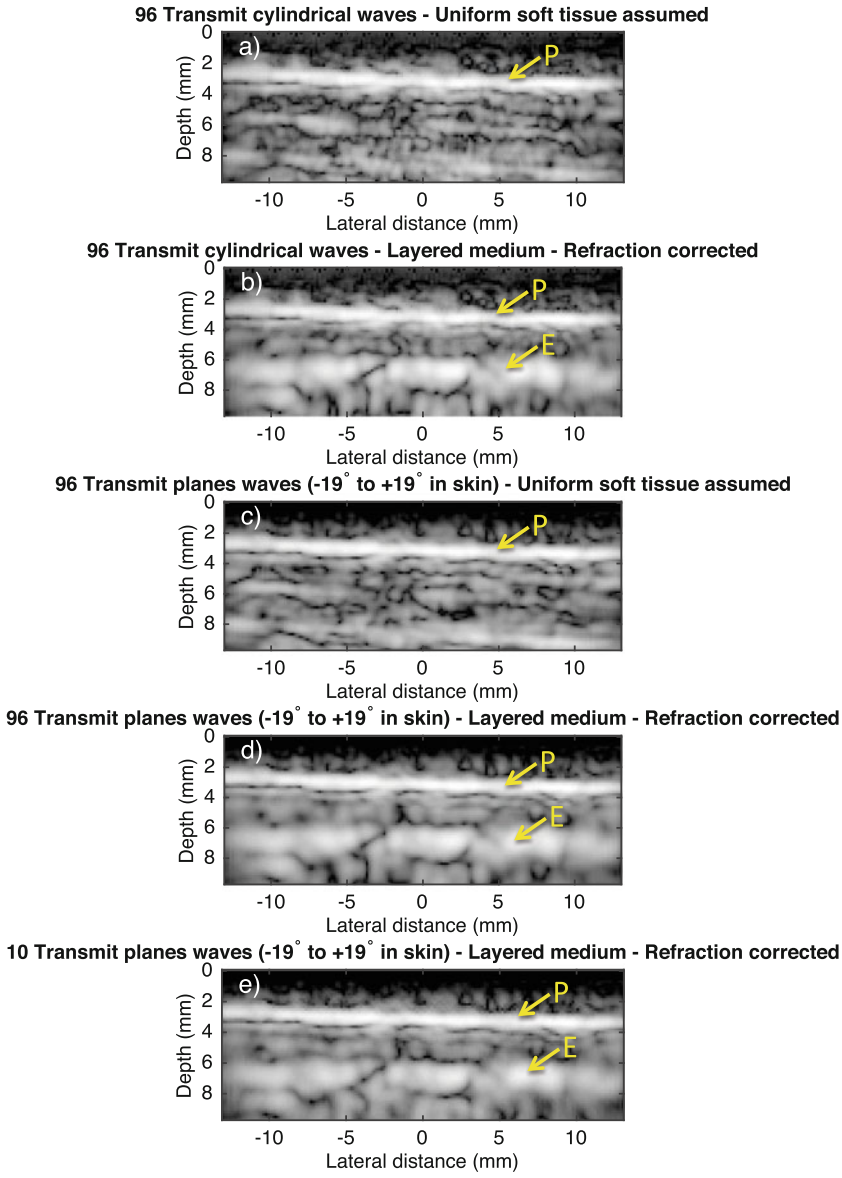

Fig. 10.14 Example of in vivo ultrasound image of the cortex of the tibial diaphysis obtained with synthetic focusing (longitudinal plane). A phased array transducer with 96 elements was used, the center frequency of the transmit short burst was 2.5 MHz. (**a**) and (**b**) transmission of 96 cylindrical waves (single element excitation). (**c**) and (**d**) transmission of 96 steered plane waves with different steering angles. (**e**) transmission of only 10 steered plane waves with different steering angles. (**a**) and (**c**) shows the image obtained if a homogeneous medium is assumed with a wave-speed equal to that in cutaneous tissue. (**b**), (**d**) and (**e**) are obtained with correction of refraction at the interface between soft tissue and cortical bone. The periosteum (P) and endosteum (E) are indicated with arrows. Data reprocessed from Renaud et al. (2018b)

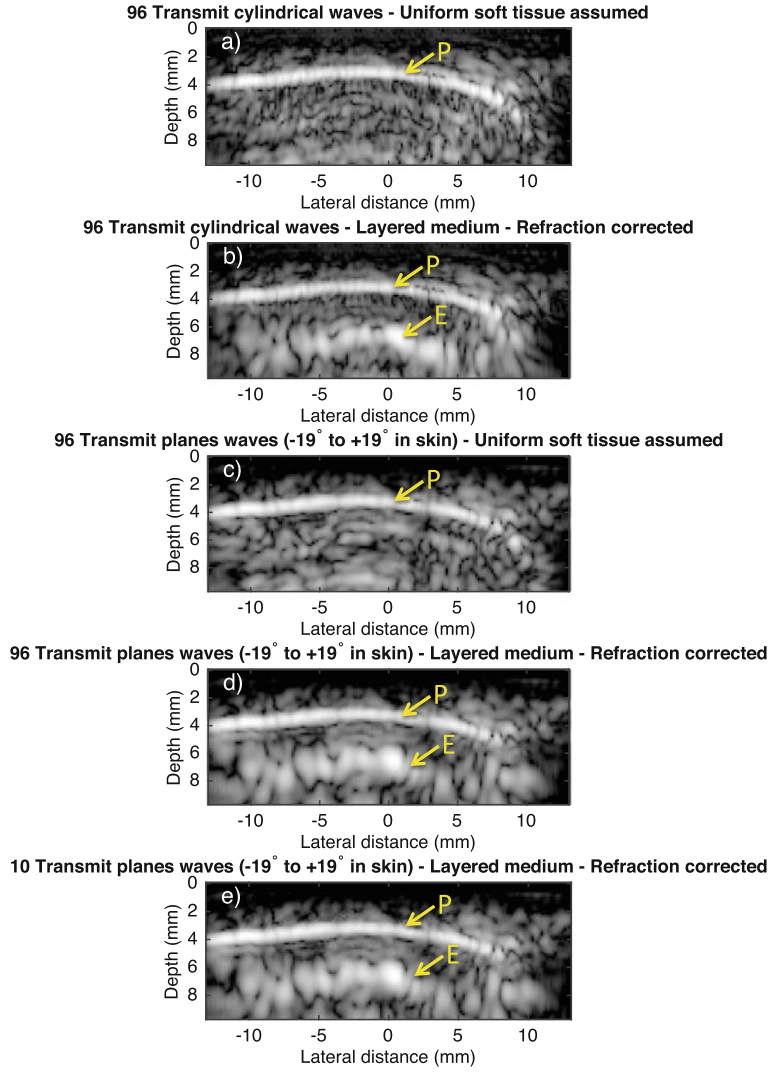

Fig. 10.15 Example of in vivo ultrasound image of the cortex of the tibial diaphysis obtained with synthetic focusing (transverse plane). A phased array transducer with 96 elements was used, the center frequency of the transmit short burst was 2.5 MHz. (**a**) and (**b**) transmission of 96 cylindrical waves (single element excitation). (**c**) and (**d**) transmission of 96 steered plane waves with different steering angles. (**e**) transmission of only 10 steered plane waves with different steering angles. (**a**) and (**c**) shows the image obtained if a homogeneous medium is assumed with a wave-speed equal to that in cutaneous tissue. (**b**), (**d**) and (**e**) are obtained with correction of refraction at the interface between soft tissue and cortical bone. The periosteum (P) and endosteum (E) are indicated with arrows. Data reprocessed from (Renaud et al., 2018b)

If one assumes a homogeneous medium (like in conventional ultrasound imaging) with the wave-speed of cutaneous tissue, the endosteum is not clearly revealed (Figs. 10.14 and 10.15, panels a and c). If refraction at the interface between cutaneous tissue and cortical bone is taken into account, the reconstructed image shows clearly the endosteum in the longitudinal and transverse images.

10.6 Real-Time Imaging of the Bone Cortex

10.6.1 Choice of the Reconstruction Technique

In order to achieve real-time imaging (i.e. continuous transmission and recording with the probe allowing reconstruction and display of several images per second), it was necessary to select the simplest reconstruction method that is nonetheless able to address the relevant Physics at stake when imaging cortical bone with ultrasound. Seismologist have developed a large number of imaging techniques with varying complexity (Etgen et al., 2009). Among them, Kirchhoff migration (called delay-and-sum in medical ultrasound) is the simplest reconstruction algorithm, and it can take into account refraction and wave-speed anisotropy. Kirchhoff migration was therefore chosen for real-time imaging of the bone cortex (Renaud et al., 2018a).

The procedure for imaging the cortex consists of three main steps:

1. Image reconstruction in cutaneous tissue until periosteum (delay-and-sum)
2. Segmentation of the periosteum (Dijkstra algorithm) and parabolic fitting of the interface
3. Image reconstruction in cortical bone until endosteum (delay-and-sum)

Even if an analytical formula of travel time can be obtained for the geometry considered here, it is actually faster to estimate the travel time numerically with an iterative approach. For instance, the travel time for a wave to propagate from a point in the cortex to the element of the probe array can be estimated with two-point ray tracing relying on Fermat's principle. The travel time along a ray path from one point to another has an extremum value which is a minimum. This minimum can be numerically estimated with Brent's method (Press et al., 2002). Details about the segmentation of the periosteum based on Dijkstra's technique can be found in (Renaud et al., 2018b, 2020). If the shape of the interface is complicated, and therefore cannot be locally approximated with a parabola, the travel times can be computed by solving the Eikonal equation with a finite-difference method (see for instance Shearer (2009) and Podvin and Lecomte (1991)) or with a fast marching technique (Sethian, 1999).

Finally, computational time can be reduced by using a small number of transmit unfocused beams. As shown in Figs. 10.14 and 10.15, the transmission of 10 steered plane waves can provide satisfying image quality.

10.6.2 Model of Weak Transverse Isotropy

Kirchhoff migration requires a velocity model of the region of interest as input. In order to reduce computational time, we proposed to describe the region of interest as a layered medium (cutaneous tissue, cortical bone, marrow), with interfaces approximated with parabolas. The wave-speed in each homogeneous layer is required for defining the velocity model, it is either assumed from a priori knowledge or estimated prior to imaging with the approach described in Sect. 10.7. Unlike cutaneous tissue and marrow, the compression wave-speed in cortical bone cannot be defined with a single scalar value since there exists wave-speed anisotropy (in a longitudinal plane). As discussed in Sect. 10.3, elastic anisotropy of cortical bone is well described with transverse isotropy. Equation 10.1 can be used for implementing Kirchhoff migration, but we adopted a weak-anisotropy simplification proposed by seismologists (Thomsen, 1986) to reduce computational time. If $|\delta^*| \ll 1$ and $|\varepsilon| \ll 1$, after full linearization of Eqs. 10.1 and 10.3, the group velocity of a compression wave V_P can be written as:

$$V_P(\phi) = V_P^{axial} - (V_P^{axial} - V_P^{radial}) \times \left[\xi \sin^2(\phi)\cos^2(\phi) + \cos^4(\phi)\right] \tag{10.13}$$

ϕ is the group angle. $V_P^{radial} = \sqrt{C_{11}/\rho}$ is the compression wave-speed in the plane of isotropy of cortical bone. $V_P^{axial} = \alpha_0 = \sqrt{C_{33}/\rho}$ is the compression wave-speed in the direction of the symmetry axis of cortical bone. ξ is an anisotropy form parameter. Even though the conditions $|\delta^*| \ll 1$ and $|\varepsilon| \ll 1$ are not properly fulfilled (see Fig. 10.6), we showed that Eq. 10.13 allows reconstruction of the bone cortex with satisfying accuracy (Renaud et al., 2018b), and it is computationally efficient for real-time imaging. For material characterization however, the model of exact transverse isotropy (Eq. 10.1) is recommended (see Sect. 10.7) because the elastic anisotropy of cortical bone is moderate, rather than weak.

10.7 The Autofocus Method for Measuring the Wave-Speed in a Layered Medium

10.7.1 Principle of the Autofocus Method

The rationale of the autofocus approach is simple: a reconstructed ultrasound image shows optimal quality (intensity and sharpness) if the wave-speed model used during image reconstruction is correct. Therefore the wave-speed can be searched by looking for the value that maximizes image intensity and sharpness. This idea was first introduced in medical ultrasound for aberration correction in soft tissues (Anderson et al., 2000; Napolitano et al., 2006; Nock et al., 1989; Trahey et al., 1990) and later for improving the quality of photoacoustic images (Treeby et al., 2011). We recently proposed to apply the autofocus approach to specular reflections at the outer and inner surfaces of the cortex of a long bone to estimate the anisotropy of compression and shear wave-speeds in cortical bone (Renaud et al., 2018b, 2020).

10.7.2 Point Scatterer or Interface?

Let us first consider a medium with only small heterogeneities (smaller than the wavelength) that can be described with a uniform wave-speed. It can be shown that the autofocus approach can be applied to echo signals recorded after the transmission of a single unfocused beam, in order to estimate the wave-speed of this medium. Each point target (each heterogeneity) generates an echo signal with arrival times at the elements of the probe array that describe a hyperbola. As mentioned previously, the delay-and-sum algorithm operates like a propagation of the recorded echo signals backward in time (or backward in depth) (Liu and Waag, 1997; Scales, 1995). Optimal focusing of the recorded data occurs if the wave-speed used during image reconstruction is correct. In this case, the center of the point spread function (for each small heterogeneity) in the reconstructed image is located at the true spatial coordinates of the "point-like" scatterers in the medium. Figure 10.16 illustrates the autofocus technique applied to a single point scatterer with the transmission of three steered plane waves.

However, with the transmission of a single unfocused beam, the autofocus method fails if the scatterer is a large interface. Indeed, optimal image quality will be found for a wave-speed value that is not the true wave-speed in the medium. In particular, the wave-speed value that produces maximum image intensity depends on the size of the receive aperture, while it should not. This is because the reconstruction algorithm operates similar to a back-propagation of the recorded echo signal. As a result, the reconstructed image shows maximum intensity when the depth of the interface in the image is close to the natural focal distance of the receive aperture. Most sharpness metrics will also be incapable of retrieving the correct wave-speed.

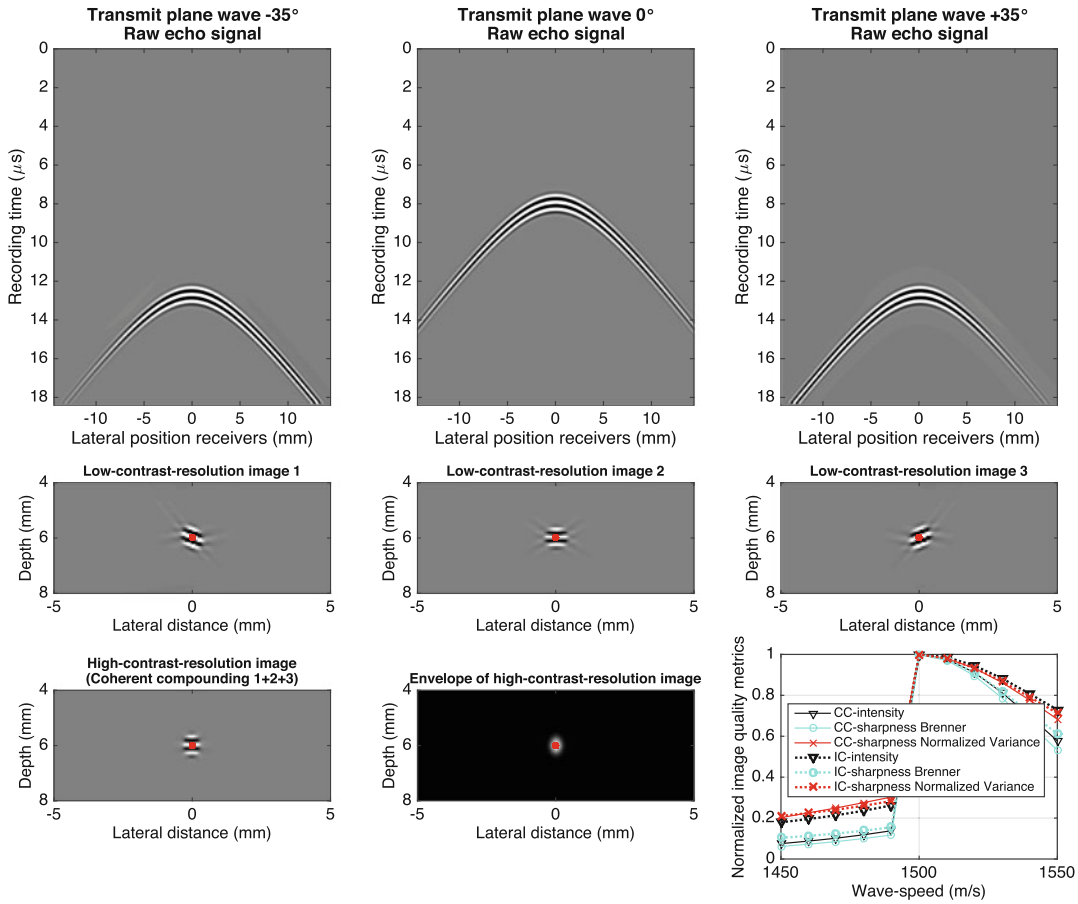

Fig. 10.16 The autofocus method applied to a single point scatterer at 6 mm depth (synthetic data generated with k-wave (Treeby et al., 2012)). Three plane waves are transmitted with steering angles of −35°, 0° and +35°. The three metrics of image quality, calculated on the envelope of the high-contrast-resolution image, are able to recover the true wave-speed (1500 m/s), if the high-contrast-resolution image is computed with coherent compounding (CC) or with incoherent compounding (IC). The red dot indicates the true position of the point target

This limitation can be overcome by transmitting multiple unfocused beams and compounding during image reconstruction. For an ultrasound frequency of 2.5 MHz, we showed that the periosteum and endosteum of the cortex of a long bone generate specular reflections with an amplitude that exceeds that of echo signals produced by diffuse scattering (Renaud et al., 2018b, 2020). Using multiple transmit cylindrical beams, it was possible to estimate the wave-speed in the tissue region overlaying the interface. Because the interface is insonified by multiple unfocused transmit beams, a given part of the interface appears in several low-contrast-resolution images. During compounding, low-contrast-resolution images will add up and create a high-contrast-resolution image with maximum intensity and sharpness only if the wave-speed used in the delay-and-sum algorithm is correct. Figure 10.17 illustrates the autofocus technique applied to an interface with the transmission of three steered plane waves. In this simple configuration, the low-contrast-resolution images and the high-contrast-resolution image look exactly the same.

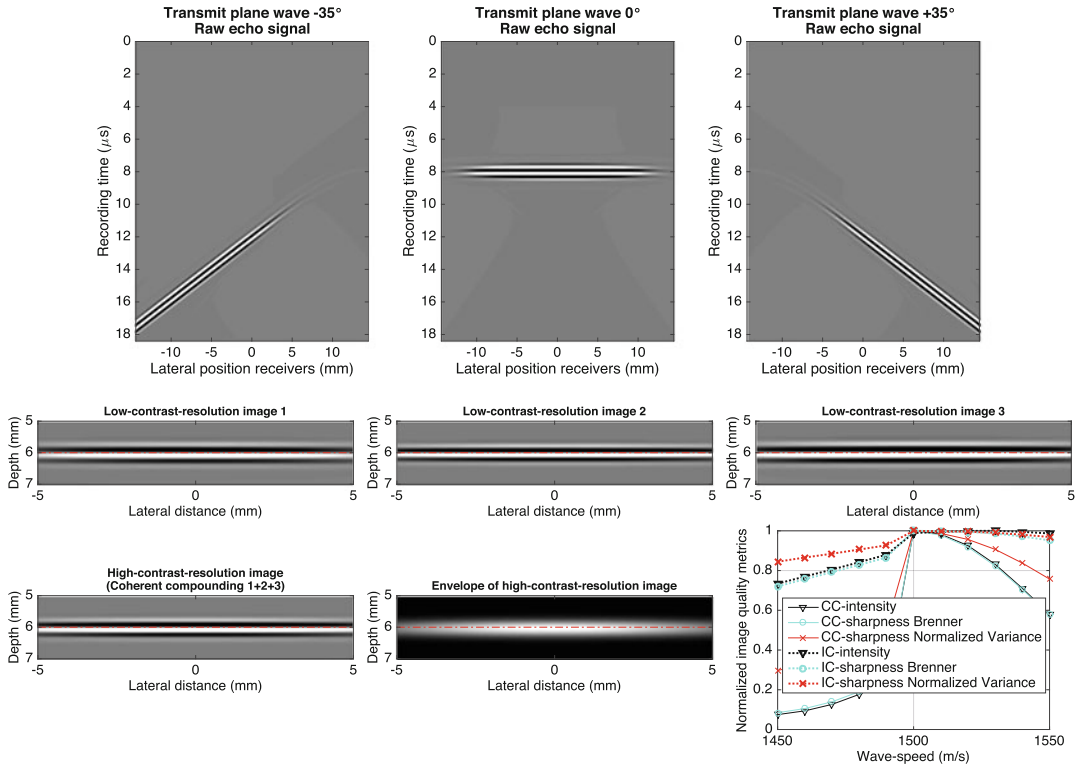

Fig. 10.17 The autofocus method applied to an interface at 6 mm depth with subcritical incidence (synthetic data generated with k-wave (Treeby et al., 2012)). The wave-speed is 1500 m/s above the interface and 1550 m/s underneath. Three plane waves are transmitted with steering angles of −35°, 0° and +35°. The three metrics of image quality, calculated on the envelope of the high-contrast-resolution image, are able to recover the true wave-speed (1500 m/s), if the high-contrast-resolution image is computed with coherent compounding (CC) or with incoherent compounding (IC). The red dash-dotted line indicates the true position of the interface

10.7.3 Coherent or Incoherent Compounding?

We would like now to address the following question: shall one use coherent or incoherent compounding? Incoherent compounding refers to the summation of the low-resolution images (obtained with a set of transmit unfocused beams) after computing their envelopes (Montaldo et al., 2009). Coherent compounding refers to the summation of the low-resolution images without computing their envelopes first.

If the phase of the waveform is constant within the wavefront recorded by the probe array, then coherent compounding is advantageous since it leverages the constructive or destructive phase interferences. Optimal constructive interferences between the low-contrast-resolution images occur only if the wave-speed is correct, which results in a high-contrast-resolution image with maximum intensity and sharpness. This situation is encountered for medium containing heterogeneities smaller than the wavelength and/or interfaces between layers with only slightly different wave-speeds. If the wave-speeds in two adjacent layers are very different (like cortical bone and adjacent soft tissue), there exists a critical value for the angle of incidence at the interface above which the reflection and transmission coefficients can take complex values. As a result, the phase of the reflected or transmitted wave is changed. In this situation, coherent compounding leads to biased estimates of the wave-speed, thus it is recommended to apply the autofocus method by adding up the envelope of the low-contrast-

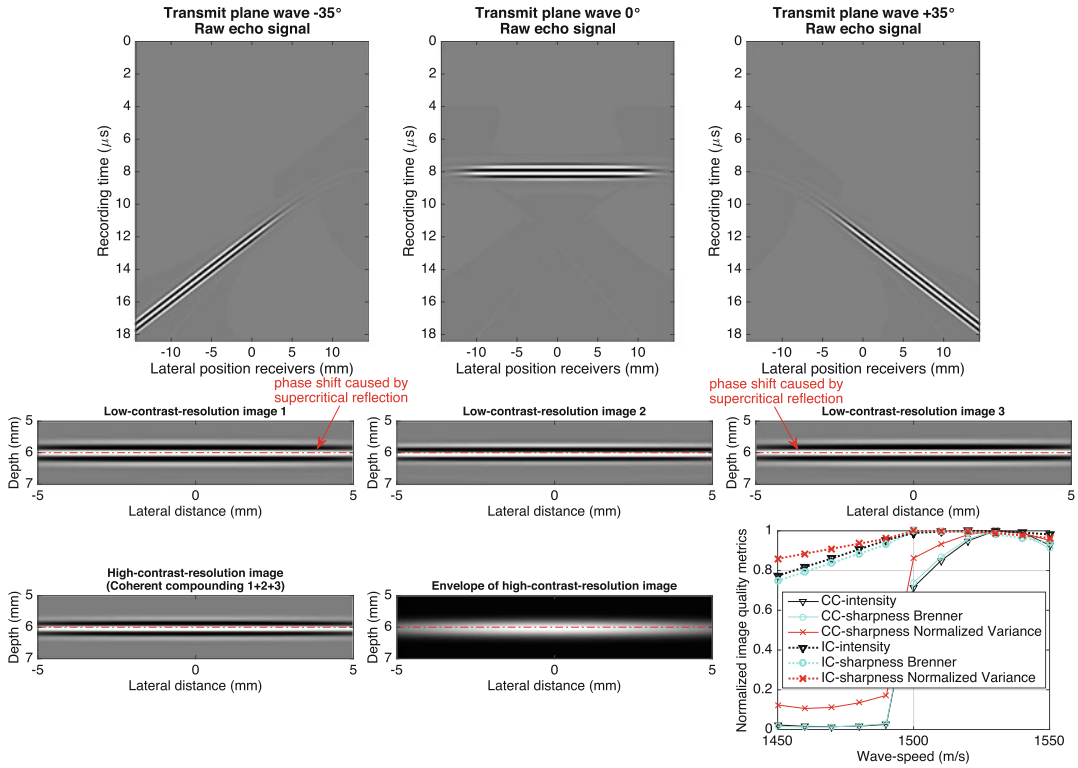

Fig. 10.18 The autofocus method applied to an interface at 6 mm depth with supercritical incidence (synthetic data generated with k-wave (Treeby et al., 2012)). The wave-speed is 1500 m/s above the interface and 4000 m/s underneath. Three plane waves are transmitted with steering angles of −35°, 0° and +35°. An incidence angle of 35° exceeds the critical angle (22°). The three metrics of image quality, calculated on the envelope of the high-contrast-resolution image, are not able to recover the true wave-speed (1500 m/s) with coherent compounding (CC), because of the phase shift created by supercritical specular reflection with transmit steering angles of −35° and +35° (see low-contrast-resolution images). However incoherent compounding (IC) provides an estimate with a small error. The red dash-dotted line indicates the true position of the interface

resolution images (incoherent compounding). Figure 10.18 illustrates the autofocus technique applied to an interface with the transmission of three steered plane waves. The transmit steering angles of −35° and +35° exceed the critical angle (22°), as a consequence the echo signal reflected at the interface is phase shifted. While coherent compounding leads to a biased estimate of the wave-speed (2% error), incoherent compounding provides a better estimate with a smaller error (0.5%).

Interestingly, the autofocus approach implemented with coherent compounding is similar to Migration Velocity Analysis (MVA) in seismology (see for instance Chauris and Noble (2001)). Its aim is to estimate a velocity model in the image domain, relying on the principle that the image of an interface, reconstructed with different sources and/or receivers should be consistent if the velocity model is correct.

10.7.4 Application to Cortical Bone: Measurement of P-Wave and SV-Wave Velocity Anisotropy

If our goal is now tissue characterization, one may want to measure ultrasound wave-speed and its anisotropy, since they are determined by the elasticity, mass density and the structural organization of the material. We have seen in Sect. 10.3 that the elastic anisotropy of cortical bone is well

described with a model of transverse isotropy. The anisotropy of the phase velocity of a quasi compression wave and a quasi shear wave with vertical polarization is described by a model with four parameters α_0, β_0, ε and δ^* (Eqs. 10.1, 10.2, and 10.3). We recently proposed a procedure to estimate these four parameters (Renaud et al., 2020), it is here briefly explained. Figure 10.19 summarizes the procedure.

The very first step consists in estimating the compression wave-speed in the soft tissue between the ultrasound probe and the bone with the autofocus method. Next the first parameter α_0 is measured with the head-wave velocity, a method borrowed from seismologists (Telford et al., 1990a). If the probe array is aligned with the bone axis, a cylindrical wave transmission with the most left element first, and then with the most right element, allows one to measure the wave-speed along the periosteum, which equals α_0 if the symmetry axis of cortical bone is exactly parallel to the periosteum. The signal processing and calculation of the head-wave velocity is straightforward if the periosteum is locally flat in the longitudinal plane. The two single-element transmissions are used to correct the effect of an angle between the transducer array and the periosteum.

The last three parameters can be estimated with the autofocus approach. We proposed to leverage the hexagonal symmetry of the material by acquiring echo signals in response to unfocused transmit beams in two planes: a plane normal to the symmetry axis and a plane parallel to the symmetry axis. In the plane normal to the symmetry axis (transverse plane), the ultrasound wave-speed is isotropic. The wave-speed can therefore be estimated with the autofocus method; the transverse image of the bone cortex is reconstructed for different values of the wave-speed, an estimate of the true wave-speed is the value that maximizes the intensity and sharpness of the image. The step would typically exploit compression waves, and lead to an estimate of $V_{P\ radial} = \sqrt{C_{11}/\rho}$. Thus $\varepsilon = (V_{P\ radial}^2 - \alpha_0^2)/(2\alpha_0^2)$ can be calculated. The last two parameters β_0 and δ^* can be estimated with the data recorded in the longitudinal plane. As shown in Eqs. 10.1, 10.2, and 10.3, the phase velocities of a quasi compression wave and a quasi shear wave with vertical polarization are coupled. We proposed in (Renaud et al., 2020) to take advantage of the four ray paths depicted in Fig. 10.8 and apply the autofocus approach to a composite image. This composite image is created by incoherent summation of four images reconstructed with the ray paths PPPP, PSSP, PSPP and PPSP. Coherent compounding is not used here because each image type has a different spatial frequency content (caused by the different wave-speeds used during image reconstruction). If the values of Thomsen's parameters are correct, spatial co-localization of the endosteum occurs in the four types of image, because PPPP, PSPP, PPSP and PSSP paths are all generated by a reflection at the same interface (endosteum). Thus the longitudinal composite image of the bone cortex is reconstructed for different values of β_0 and δ^*, the pair of values that maximizes the intensity and sharpness of the composite image represents our estimates.

10.8 Measuring Intracortical Blood Flow with Ultrasound Imaging

Intraosseous blood circulation is thought to have a key role in bone growth and remodeling, and in the development of bone disorders (Lafage-Proust et al., 2015; Ramasamy et al., 2016; Laroche, 2002; Marenzana & Arnett, 2013; McCarthy, 2006). However, it is rarely considered in clinical practice due to the absence of a suitable non-invasive measurement technique. Therefore we have recently proposed to assess blood perfusion in the cortex of a long bone with intraosseous ultrasound imaging (Salles et al., 2020). The approach capitalizes on the work described above, i.e. the reconstruction of a faithful anatomical ultrasound image of the bone cortex. By repeating the acquisition scheme hundreds of times per second for reconstructing an ensemble of images, information on blood flow can be inferred from the time-variant components of the ultrasound image of the cortex, which can be extracted with singular value

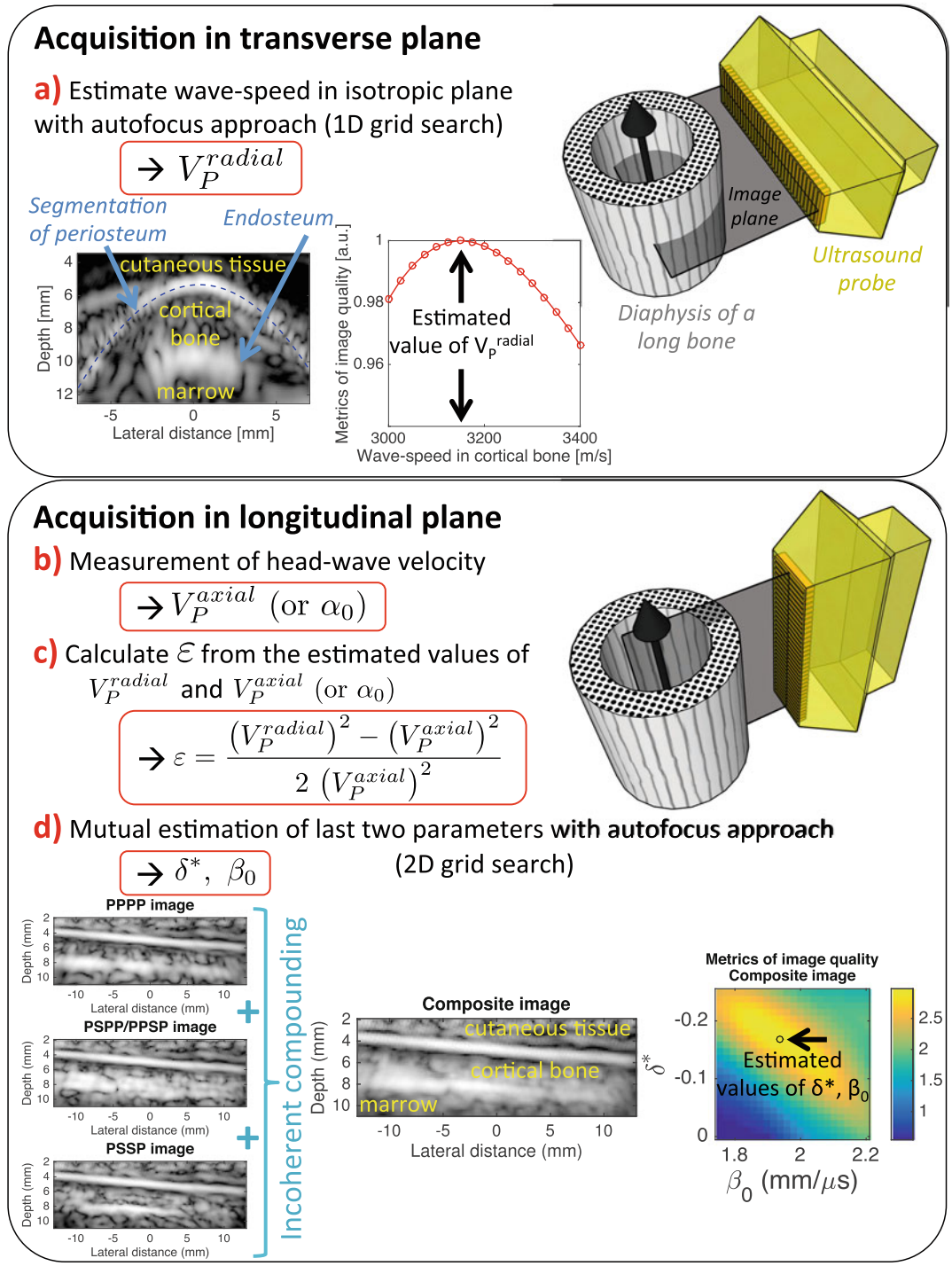

Fig. 10.19 Procedure for measuring the four parameters of the model of exact transverse isotropy at the diaphysis of a long bone

decomposition (SVD) (Demené et al., 2015). Figure 10.20 describes the methodology used in vivo to measure blood flow in the cortex of the tibial diaphysis.

The so-called "Power Doppler" signal and "signed Power Doppler" signals (see for instance Osmanski et al., 2012) were calculated for each image pixel. The magnitude of the "Power Doppler" signal is proportional to the volume of blood in motion, but it does not provide an absolute physical measurement of blood flow rate or velocity. However it is possible to calculate "signed Power Doppler" to obtain directional information along the axis of the ultrasound beam. In our recent experiments in healthy volunteers (Salles et al., 2021), we used a phased-array transducer with a center ultrasound frequency of 2.5 MHz (Fig. 10.20).

The ultrasound transducer was aligned with the axis of the tibia (longitudinal image). The ultrasound beam axis was therefore nearly normal to the long bone axis. As a result, we were able to sense blood flow primarily in a direction normal to the long bone axis (centrifugal or centripetal blood circulation through the cortex). Figure 10.20 shows, at a given image pixel, that our measurements reveal pulsatile and predominantly centrifugal blood flow, i.e. from the medullary cavity to the outside of the bone. Pulsatility and predominantly centrifugal blood flow remain after spatial averaging over the cortex (Fig. 10.21). This finding is in agreement with most experiments on animal models and scarce observations in humans (Bridgeman & Brookes, 1996), although there is still some debate on the direction of arterial and venous blood flow through the cortex (Asghar et al., 2020; Grüneboom et al., 2019). The Power Doppler signal shows little sensitivity to the angle between the ultrasound beam axis and the flow direction (Rubin, 1999). Because Haversian canals host blood vessels, blood in the diaphyseal cortex also circulates in the direction of the long bone axis. Therefore the Power Doppler signal measured in our experiments likely contains information about blood circulation in Haversian canals.

10.9 Conclusion

This book chapter has shown the many possibilities offered by intraosseous ultrasound imaging, including the measurement of the cortical thickness, the characterization of tissue microstructure via the estimation of the ultrasound wave-speed and its anisotropy, and the measurement of intracortical blood flow. Bones have complex three-dimensional geometries. However the geometry of the diaphysis of a long bone is locally rather simple, with a nearly tubular shape. We have shown that longitudinal and transverse views of the cortex can be reconstructed by using a clinical cardiac phased-array transducer. This ultrasound transducer is made of a linear array of piezoelectric elements, with an element height in the elevation direction close to 13 mm. While the spatial sampling was excellent in the azimutal direction thanks to the array spatial periodicity of half a wavelength (0.3 mm), the recorded backscattered wavefronts were not optimally spatially sampled in the elevation direction. This limitation can be overcome with the use of a matrix array transducer, this technology is now mature and should be considered in future research on intraosseous ultrasound imaging.

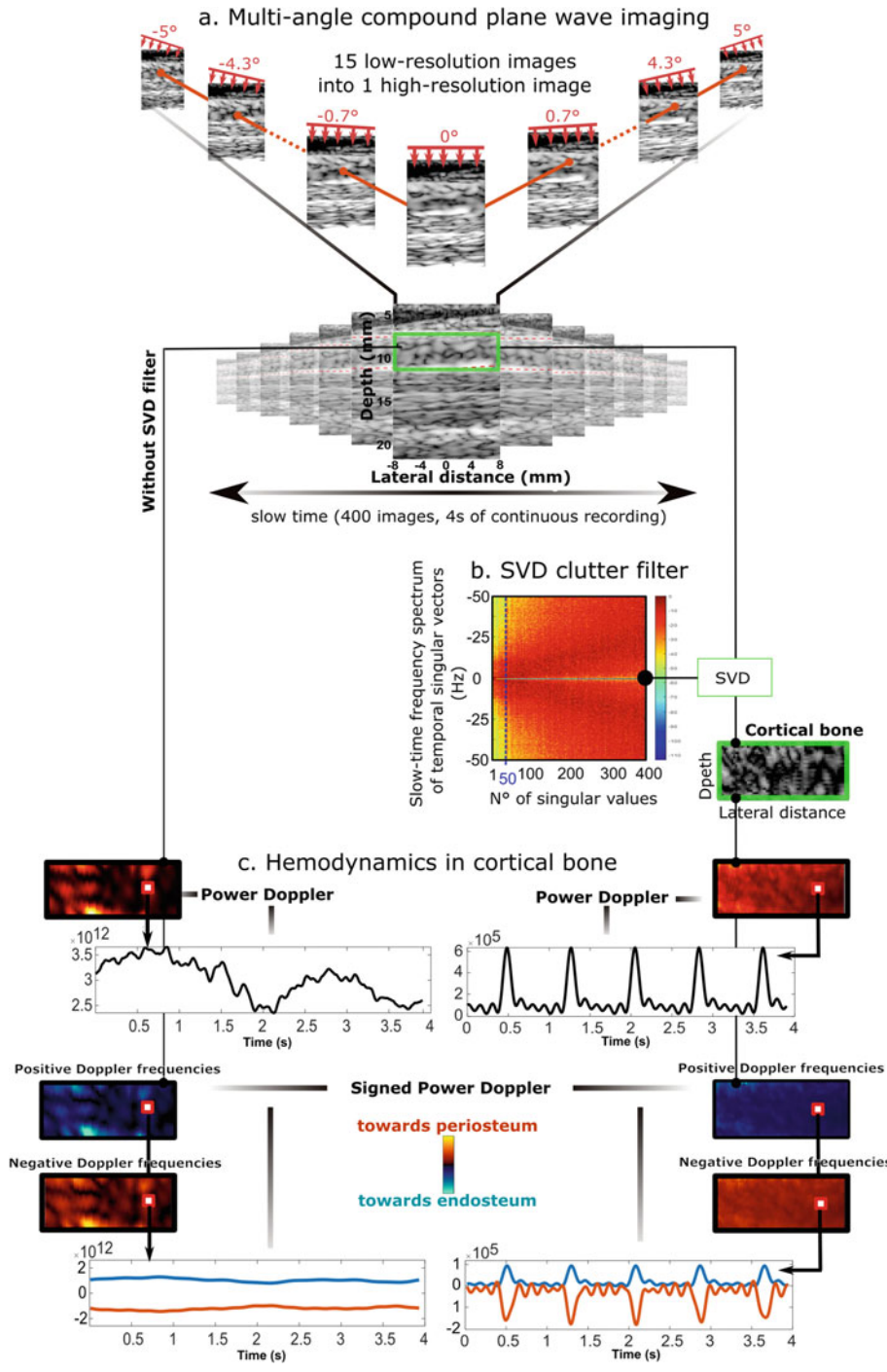

Fig. 10.20 Method for measuring blood flow in the cortex of a long bone. The ultrasound probe was positioned on the medial surface of the tibia of the volunteer, in the middle of the diaphysis. The resulting "power Doppler" signal is shown at a pixel in the image of the cortex. Pulsatile and predominantly centrifugal blood flow is measured

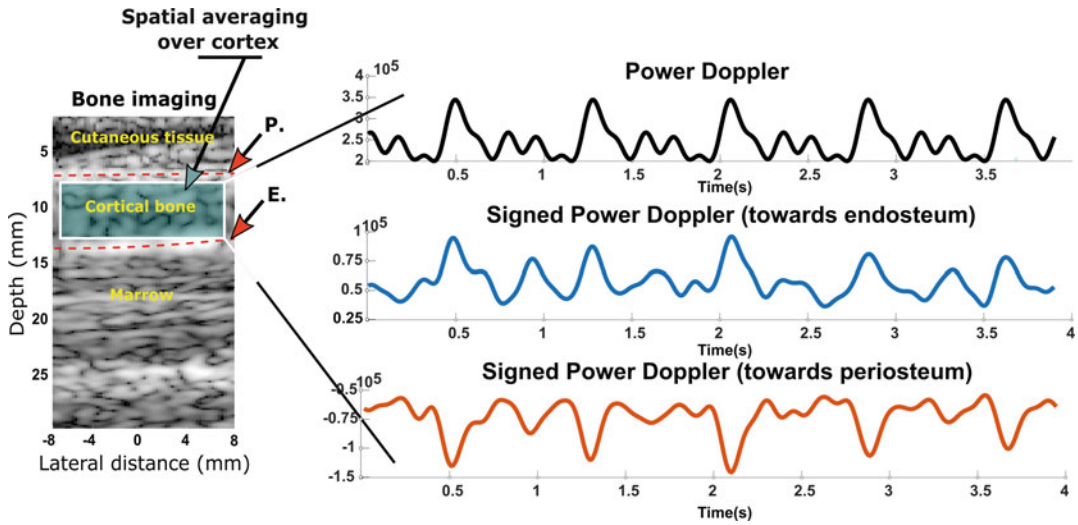

Fig. 10.21 Pulsatility and predominantly centrifugal blood flow remain after spatial averaging over the tibial cortex. The periosteum (P) and endosteum (E) are indicated with arrows

References

Aki, K., Richards, P. G. (2002). *Quantitative Seismology* (2nd ed.). University Science Books.

Anderson, M. E., McKeag, M. S., & Trahey, G. E. (2000). The impact of sound speed errors on medical ultrasound imaging. *The Journal of the Acoustical Society of America*, *107*(6), 3540–3548.

Asghar, A., Narayan, R. K., Kumar, A., & Naaz, S. (2020). The transcortical vessel is replacement of cortical capillary or a separate identity in diaphyseal vascularity. *Anatomy & Cell Biology*, *53*(1), 107–110.

Ashman, R. B., Cowin, S. C., Van Buskirk, W. C., & Rice, J. C. (1984). A continuous wave technique for the measurement of the elastic properties of cortical bone. *Journal of Biomechanics*, *17*(5), 349–361.

Auld, B. (1973a). *Acoustic fields and waves in solids - Volume 1*. John Wiley and Sons.

Auld, B. (1973b). *Acoustic fields and waves in solids - Volume 2*. John Wiley and Sons.

Beltrame, V., Stramare, R., Rebellato, N., Angelini, F., Frigo, A. C., & Rubaltelli, L. (2012). Sonographic evaluation of bone fractures: a reliable alternative in clinical practice? *Clinical Imaging*, *36*(3), 203–208.

Bercoff, J., Montaldo, G., Loupas, T., Savery, D., Mézière, F., Fink, M., & Tanter, M. (2011). Ultrafast compound doppler imaging: providing full blood flow characterization. *IEEE Transactions on Ultrasonics, Ferroelectrics, and Frequency Control*, *58*(1), 134–147.

Bernard, S., Schneider, J., Varga, P., Laugier, P., Raum, K., & Grimal, Q. (2016). Elasticity-density and viscoelasticity-density relationships at the tibia mid-diaphysis assessed from resonant ultrasound spectroscopy measurements. *Biomech Model Mechanobiol*, *15*(1), 97–109.

Bossy, E., Talmant, M., & Laugier, P. (2002). Effect of bone cortical thickness on velocity measurements using ultrasonic axial transmission: A 2d simulation study. *The Journal of the Acoustical Society of America*, *112*(1), 297–307.

Brekhovskikh, L., & Godin, O. (1992). *Acoustics of layered media II: Point sources and bounded beams. Wave phenomena* (Vol. 10). Springer.

Bridgeman, G., & Brookes, M. (1996). Blood supply to the human femoral diaphysis in youth and senescence. *Journal of Anatomy*, *188*(Pt 3), 611–621.

Cai, X., Peralta, L., Giron, A., Helfen, L., Olivier, C., Peyrin, F., Laugier, P., & Grimal, Q. (2017). Cortical bone elasticity measured by resonant ultrasound spectroscopy is not altered by defatting and synchrotron x-ray imaging. *Journal of the Mechanical Behavior of Biomedical Materials*, *72*, 241–245.

Cai, X., Follet, H., Peralta, L., Gardegaront, M., Farlay, D., Gauthier, R., Yu, B., Gineyts, E., Olivier, C., Langer, M., Gourrier, A., Mitton, D., Peyrin, F., Grimal, Q., & Laugier, P. (2019). Anisotropic elastic properties of human femoral cortical bone and relationships with composition and microstructure in elderly. *Acta Biomaterialia*, *90*, 254–266.

Cai, X., Peralta, L., Brenner, R., Iori, G., Cassereau, D., Raum, K., Laugier, P., & Grimal, Q. (2020). Anisotropic elastic properties of human cortical bone tissue inferred from inverse homogenization and resonant ultrasound spectroscopy. *Materialia*, *11*, 100730.

Carcione, J. (2014). *Wave fields in real media: Wave propagation in anisotropic, anelastic, porous and electromagnetic media* (3rd ed.). Elsevier Science.

Cerveny, V. (2001). *Seismic ray theory*. Cambridge University Press.

Chauris, H., & Noble, M. (2001). Two-dimensional velocity macro model estimation from seismic reflection data by local differential semblance optimization: applications to synthetic and real data sets. *Geophysical Journal International*, *144*(1), 14–26.

Demené, C., Deffieux, T., Pernot, M., Osmanski, B. F., Biran, V., Gennisson, J. L., Sieu, L. A., Bergel, A., Franqui, S., Correas, J. M., & Cohen, I. (2015). Spatiotemporal clutter filtering of ultrafast ultrasound data highly increases doppler and f-ultrasound sensitivity. *IEEE Transactions on Medical Imaging*, *34*(11), 2271–2285.

Etgen, J., Gray, S., & Zhang, Y. (2009). An overview of depth imaging in exploration geophysics. *Geophysics*, *74*(6), WCA5–WCA17.

Granke, M., Grimal, Q., Saïed, A., Nauleau, P., Peyrin, F., & Laugier, P. (2011). Change in porosity is the major determinant of the variation of cortical bone elasticity at the millimeter scale in aged women. *Bone*, *49*(5), 1020–1026.

Grüneboom, A., Hawwari, I., Weidner, D., Culemann, S., Müller, S., Henneberg, S., Brenzel, A., Merz, S., Bornemann, L., Zec, K., Wuelling, M., Kling, L., Hasenberg, M., Voortmann, S., Lang, S., Baum, W., Ohs, A., Kraff, O., Quick, H. H., Jäger, M., Landgraeber, S., Dudda, M., Danuser, R., Stein, J. V., Rohde, M., Gelse, K., Garbe, A. I., Adamczyk, A., Westendorf, A. M., Hoffmann, D., Christiansen, S., Engel, D. R., Vortkamp, A., Krönke, G., Herrmann, M., Kamradt, T., Schett, G., Hasenberg, A., & Gunzer, M. (2019). A network of trans-cortical capillaries as mainstay for blood circulation in long bones. *Nature Metabolism*, *1*(2), 236–250.

Holmes, C., Drinkwater, B., & Wilcox, P. (2005). Post-processing of the full matrix of ultrasonic transmit–receive array data for non-destructive evaluation. *NDT & E International*, *38*(8), 701–711.

Hoskins, P., Martin, K., & Thrush, A. (Eds.). (2019). *Diagnostic Ultrasound, Physics and Equipment* (3rd ed.). CRC Press.

Jensen, J., Nikolov, S., Gammelmark, K., & Pedersen, M. (2006). Synthetic aperture ultrasound imaging. *Ultrasonics*, *44*(Supplement), e5–e15.

Lafage-Proust, M. H., Roche, B., Langer, M., Cleret, D., Bossche, A., Olivier, T., & Vico, L. (2015). Assessment of bone vascularization and its role in bone remodeling. *BoneKEy Reports*, *4*, 1–8.

Laroche, M. (2002). Intraosseous circulation from physiology to disease. *Joint Bone Spine*, *69*(3), 262–269.

Liu, D. L., & Waag, R. C. (1997). Propagation and backpropagation for ultrasonic wavefront design. *IEEE Transactions on Ultrasonics, Ferroelectrics, and Frequency Control*, *44*(1), 1–13.

Marenzana, M., & Arnett, T. (2013). The key role of the blood supply to bone. *Bone Research*, *1*, 203–215.

McCarthy, I. (2006). The physiology of bone blood flow: A review. *Journal of Bone & Joint Surgery*, *88*(suppl_3), 4–9.

Montaldo, G., Tanter, M., Bercoff, J., Benech, N., & Fink, M. (2009). Coherent plane-wave compounding for very high frame rate ultrasonography and transient elastography. *IEEE Transactions on Ultrasonics, Ferroelectrics, and Frequency Control*, *56*(3), 489–506.

Napolitano, D., Chou, C., McLaughlin, G., Ji, T., Mo, L., DeBusschere, D., & Steins, R. (2006). Sound speed correction in ultrasound imaging. *Ultrasonics*, *44*(Supplement), e43–e46.

Nikolov, S., & Jensen, J. A. (2002). Virtual ultrasound sources in high-resolution ultrasound imaging. In *Proc. SPIE* (Vol. 4687).

Nock, L., Trahey, G. E., & Smith, S. W. (1989). Phase aberration correction in medical ultrasound using speckle brightness as a quality factor. *The Journal of the Acoustical Society of America*, *85*(5), 1819–1833.

Osmanski, B., Pernot, M., Montaldo, G., Bel, A., Messas, E., & Tanter, M. (2012). Ultrafast doppler imaging of blood flow dynamics in the myocardium. *IEEE Transactions on Medical Imaging*, *31*(8), 1661–1668.

Parnell, W. J., & Grimal, Q. (2009). The influence of mesoscale porosity on cortical bone anisotropy. investigations via asymptotic homogenization. *Journal of The Royal Society Interface*, *6*(30), 97–109.

Podvin, P., & Lecomte, I. (1991). Finite difference computation of traveltimes in very contrasted velocity models: a massively parallel approach and its associated tools. *Geophysical Journal International*, *105*(1), 271–284.

Press, W., Teukolsky, S., Vetterling, W., & Flannery, B. (2002). *Numerical recipes in C++: The art of scientific computing*. Cambridge University Press.

Ramasamy, S. K., Kusumbe, A. P., Schiller, M., Zeuschner, D., Bixel, M. G., Milia, C., Gamrekelashvili, J., Limbourg, A., Medvinsky, A., Santoro, M. M., Limbourg, F. P., & Adams, R. H. (2016). Blood flow controls bone vascular function and osteogenesis. *Nature Communications*, *7*, 13601.

Renaud, G., Johnson, J. L., & Cassereau, D. (2018a). Real-time kirchhoff migration for ultrasound imaging of the bone cortex. In *SEG technical program expanded abstracts* (pp. 4797–4801).

Renaud, G., Kruizinga, P., Cassereau, D., & Laugier, P. (2018b). In vivo ultrasound imaging of the bone cortex. *Physics in Medicine & Biology*, *63*, 125010.

Renaud, G., Clouzet, P., Cassereau, D., & Talmant, M. (2020). Measuring anisotropy of elastic wave velocity with ultrasound imaging and an autofocus method - application to cortical bone. *Physics in Medicine & Biology*, *65*, 235016.

Rho, J. Y. (1996). An ultrasonic method for measuring the elastic properties of human tibial cortical and cancellous bone. *Ultrasonics*, *34*(8), 777–783.

Rho, J. Y., Kuhn-Spearing, L., & Zioupos, P. (1998). Mechanical properties and the hierarchical structure of bone. *Medical Engineering & Physics*, *20*(2), 92–102.

Rohrbach, D., Lakshmanan, S., Peyrin, F., Langer, M., Gerisch, A., Grimal, Q., Laugier, P., & Raum, K. (2012). Spatial distribution of tissue level properties in a human femoral cortical bone. *Journal of Biomechanics*, *45*(13), 2264–2270.

Rubin, J. M. (1999). Power doppler. *European Radiology*, *9*(3), S318–S322.

Rudy, D. J., Deuerling, J. M., Orías, A. A. E., & Roeder, R. K. (2011). Anatomic variation in the elastic inhomogeneity and anisotropy of human femoral cortical bone tissue is consistent across multiple donors. *Journal of Biomechanics*, *44*(9), 1817–1820.

Salles, S., Johnson, J. L., Clouzet, P., Vos, H., & Renaud, G. (2020). Intraosseous blood circulation: a first assessment using plane wave ultrasound imaging and transverse oscillations. In *Abstract of IEEE International Ultrasonics Symposium*.

Salles, S., Shepherd, J., Vos, H. J., & Renaud, G. (2021). Revealing intraosseous blood flow in the human tibia with ultrasound. *bioRxiv*. https://doi.org/10.1101/2021.04.12.439472

Scales, J. (1995). *Theory of seismic imaging*. Springer.

Sethian, J. A. (1999). Fast marching methods. *SIAM Review*, *41*(2), 199–235.

Shearer, P. M. (2009). *Introduction to seismology*. Cambridge University Press.

Shung, K. (2015). *Diagnostic ultrasound: Imaging and blood flow measurements* (2nd ed.). CRC Press - Taylor & Francis Group.

Szabo, T. (2013). *Diagnostic ultrasound imaging: Inside out* (2nd ed.). Academic Press.

Telford, W., Geldart, L., & Sheriff, R. (1990a). *Applied Geophysics* (2nd ed., Chap. 4). Cambridge University Press.

Telford, W. M., Geldart, L. P., & Sheriff, R. E. (1990b). *Applied Geophysics*. Cambridge University Press.

Thomsen, L. (1986). Weak elastic anisotropy. *Geophysics*, *51*(10), 1954–1966.

Trahey, G., Zhao, D., Miglin, J., & Smith, S. (1990). Experimental results with a real-time adaptive ultrasonic imaging system for viewing through distorting media. *IEEE Transactions on Ultrasonics, Ferroelectrics, and Frequency Control*, *37*(5), 418–427.

Treeby, B., Varslot, T., Zhang, E., Laufer, J., & Beard, P. (2011). Automatic sound speed selection in photoacoustic image reconstruction using an autofocus approach. *Journal of Biomedical Optics*, *16*(9), 090501.

Treeby, B. E., Jaros, J., Rendell, A. P., & Cox, B. T. (2012). Modeling nonlinear ultrasound propagation in heterogeneous media with power law absorption using a k-space pseudospectral method. *The Journal of the Acoustical Society of America*, *131*(6), 4324–4336.

Ursenbach, C., Haase, A. B., & Downton, J. E. (2005). An efficient method for AVO modeling of reflected spherical waves. In *SEG Technical Program Expanded Abstracts* (pp. 202–205).

Yoon, H. S., & Katz, J. L. (1976). Ultrasonic wave propagation in human cortical bone–ii. measurements of elastic properties and microhardness. *Journal of Biomechanics*, *9*(7), 459–464.